Open-loop control of compressible afterbody flows using adjoint methods

Philippe Meliga and Denis Sipp
ONERA/DAFE, 8 rue des Vertugadins, 92190 Meudon, France

Jean-Marc Chomaz
LadHyX, CNRS-École Polytechnique, F-91128 Palaiseau, France
(Dated: March 15, 2010)

The flow past an axisymmetric body is generically unstable to a steady and a time-periodic global instability, the latter being thought to lead the low-frequency unsteadiness of the wake even at larger Reynolds numbers. The present paper examines how the growth rate of the oscillatory unstable mode developing in the wake of bullet-shaped objects can be reduced by a steady forcing, whose effect is to modify the base flow. The use of the compressible Navier–Stokes equations allows to consider control through steady mass, momentum and heat forcing applied in the bulk and at the wall. To do so, we extend to compressible flows and axisymmetric geometries the method first proposed by Hill (*NASA Tech. Rep.* 103858, 1992) to analyze the control of the two-dimensional mode of the incompressible cylinder wake. This method aims at evaluating the sensitivity of one particular eigenvalue to forcing by resolution of adjoint equations. Considering control at the wall, it allows to compute directly the eigenvalue gradient with respect to the wall variables. We show that the oscillating mode can be stabilized by a steady blowing at the wall (the so-called base-bleed control). Expressing the gradient as a sum of production, streamwise advection and cross-stream advection terms, we show that this stabilizing effect is due to cross-stream advection, in contradiction with the up to now accepted interpretation based on the local absolute and convective instability analysis of parallel profiles. The same technique allows to compute the gradient of the oscillatory eigenvalue to bulk mass, momentum and heat sources. Momentum control can be achieved by placing a small ring in the lee of the afterbody. Similar to the 2-D case studied by Hill, the effect of such a ring is twofold, as it induces a steady drag force which modifies the base flow, and a fluctuating drag force proportional to the perturbation momentum at the ring location. We show that the efficiency of the control can be improved by heating the ring, which then acts as an additional heat source.

I. INTRODUCTION

The transonic flow past an afterbody is dominated by the low-frequency shedding of large-scale coherent structures. This vortex-shedding may be detrimental to the engineering application, as it may induce unsteady side loads and cause flow induced vibrations. Alleviation or control of such unsteadiness is therefore required to improve the aerodynamic performances and reliability of future launch vehicles. We consider here a compressible afterbody flow at moderate Reynolds number and at a Mach number $M = 0.5$, a parameter setting which may be of practical interest for the low-density flows encountered in the stratosphere by high-altitude rockets and re-entry vehicles. In this range of Reynolds numbers, the vortex-shedding activity has been linked to an instability of helical modes of azimuthal wavenumbers $m = \pm 1$[1–3]. For the higher Reynolds numbers found at lower altitudes, vortex-shedding persists as a coherent large-scale phenomenon superimposed on the turbulent flow field[4–6], which suggests that the present results rigorously derived at moderate Reynolds numbers can carry over as a first step towards the control of the turbulent flow.

Control of vortex-shedding in the wake of bluff bodies has been a subject of great interest in the last decades (see Choi[7] for a review). In this study, we focus on open-loop methods, which rely on the simple idea that the dominant dynamical processes can be altered by imposing a steady modification of the flow conditions. Simple bulk strategies are based on the action of a small secondary body, referred to as the control device, placed past the main body whose unsteadiness is to be controlled. For instance, a suitably positioned control cylinder can yield a complete suppression of unsteadiness in the flow past a circular cylinder[8] and in a transonic cavity flow[9]. Similarly, a small control disk mounted at the rear of an afterbody can trigger a significant reduction of drag and of the vortex-shedding activity[10,11]. Localized gas discharges acting as heat sources in the bulk have also been used to stabilize the unsteady shock wave on a truncated body equipped with a central spike[12]. In the general context of flow control, many tractable control strategies are achieved through forcing at the wall: for instance base bleed control, i.e. the injection of fluid into the wake of a bluff-body, allows to alleviate unsteadiness[13,14]. Wall cooling[15,16] and surface rugosities[17] have been used to delay the transition to turbulence in boundary-layer flows, whereas the use of surface discharges was proven fruitful to prevent flow separation[18]. However, such heuristic approaches can be extremely

time-consuming if the number of degrees of freedom is large. Indeed, the effect on the disturbance growth must be evaluated for each control setting by carrying out either experimental measurements, numerical simulations or direct stability analyses, hence motivating the development of systematical optimization techniques.

As will be demonstrated in the following, the flow under consideration is characterized by a specific sequence of bifurcations that gives credence to the interpretation of the observed intense, periodic oscillations in terms of the saturation of an unstable global mode, i.e. an eigenmode inhomogeneous in both the cross-stream and the streamwise directions. This approach, early introduced in the case of the cylinder wake flow[19,20], has been used to describe the dominant instability mechanisms at work in a wide variety of flows in complex geometry (see Theofilis[21] for a review). The so-gained information can therefore be used to derive efficient flow control strategies, as discussed for instance in the review by Collis *et al.*[22] and the references therein. The present paper considers, as recent studies did, how the dynamics of the global mode whose instability leads to vortex-shedding can be modified by a small but finite-amplitude steady forcing applied in the bulk and at the wall. To this end, a precursor study has been carried out by Hill[23], who investigated theoretically the control of the incompressible cylinder wake flow by means of a small control cylinder modeled by the drag force it exerts on the flow. Hill predicted the existence of specific flow regions where the presence of the control cylinder inhibits the vortex-shedding activity, his results exhibiting a striking agreement with that obtained experimentally by Strykowski & Sreenivasan[8]. Such an approach has known a renewed interest, as Marquet *et al.*[24] and Giannetti & Luchini[25] recently reconsidered the effect of the control cylinder at the base flow level and at the perturbation level, respectively.

This paper presents a gradient-based sensitivity formalism for the forcing of global modes governed by the compressible Navier–Stokes equations. It aims at providing a systematic method for open-loop control of afterbody flow unsteadiness viewed as a global instability, in contrast with previous studies on compressible boundary-layers relying on the parabolized approximation of the equations[26]. As in Hill[23] and Marquet *et al.*[24], the forcing acts by modifying the base flow on which the disturbances develop. Using a complementary sensitivity framework to study how small modifications of the Mach number may affect the dynamics of global modes, we have indeed shown that such a change in the base flow profiles is a key mechanism allowing to interpret the stability of compressible wake flows[27]. We use adjoint methods to compute the gradients of the eigenvalue with respect to the forcing by solving only once the state and adjoint problems, which requires a relatively 'low' computational cost. The compressible formalism includes novel bulk control strategies, such as mass and heat sources, but also forcing at the wall, which allows to obtain quantitative results for control by base bleed and wall heating and cooling. Such gradient-based control techniques are physically tractable, and have therefore potentially many practical applications. In particular, the results obtained for heat control remain valid even when the Mach number tends to zero. Moreover, the present approach can be used to provide optimal and robust control strategies by means of an iterative algorithm based on the repeated computation of the adjoint state[28].

The paper is organized as follows: the flow configuration and numerical method are presented in Sec. II-III. The base flow and disturbance equations are solved in Sec. IV, where we identify the global mode expected to trigger the onset of the periodic regime. In Sec. V, we develop the sensitivity formalism and derive the analytical expression of the gradients, also termed sensitivity functions. Forcing in the bulk is investigated in Sec. VI, where we consider successively the effect of momentum and heat sources. In the case of momentum forcing, the analysis is particularized by considering the effect of a small control ring placed at various positions in the wake, whose effect is modeled by a pure drag force. Forcing at the wall is considered in Sec. VII, where we further examine the case of base bleed. We also propose physical interpretations for the observed stabilizing effects by analyzing the base flow modification induced by the forcing.

II.   FLOW CONFIGURATION

We investigate the control of the axisymmetric flow developing in the compressible regime past the afterbody of revolution shown in Figure 1. It models a rocket shape, with a blunt trailing edge of diameter D placed into a uniform flow at zero angle of attack[10,11], and is identical to that experimentally investigated by Sevilla & Martínez-Bazàn[29], with a total length $l = 9.8D$ and an ellipsoidal nose of aspect ratio $3:1$. The problem is formulated using a standard cylindrical coordinate system (r, θ, z) of axis Γ_a, whose origin is taken at the center of the body base.

The fluid is a variable density, compressible, perfect gas with constant specific heats c_v and c_p,
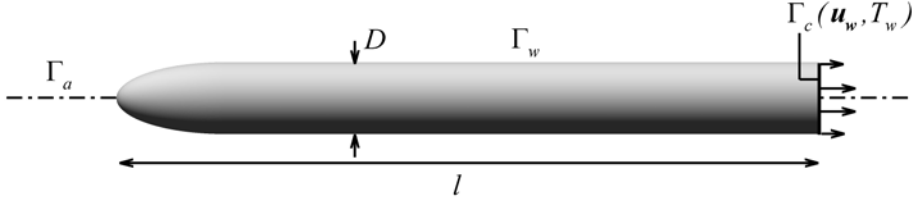
Figure 1: Configuration under study: the slender body of revolution has a diameter D and a total length $l = 9.8D$.

thermal conductivity κ, and dynamic viscosity μ, related by a ratio of specific heats $\gamma = 1.4$ and a Prandtl number $Pr = 1$. The fluid motion is described by a state vector formulated either in terms of non-conservative variables as $\boldsymbol{q} = (\varrho, \boldsymbol{u}, \Theta, p)^T$, or in terms of conservative variables as $\boldsymbol{q} = (\varrho, \varrho\boldsymbol{u}, \varrho\Theta, p)^T$, where ϱ is the density, Θ the temperature, p the pressure and $\boldsymbol{u} = (u, v, w)^T$ the three-dimensional velocity field, with u, v and w its radial, azimuthal and streamwise components. We use here non-conservative variables, so that $\boldsymbol{q}$ obeys the compressible Navier–Stokes equations formulated as

$$\partial_t \varrho + \varrho \boldsymbol{\nabla} \cdot \boldsymbol{u} + \boldsymbol{u} \cdot \boldsymbol{\nabla}\varrho = j \,, \tag{1a}$$

$$\varrho\partial_t \boldsymbol{u} + \varrho\boldsymbol{\nabla}\boldsymbol{u} \cdot \boldsymbol{u} + \frac{1}{\gamma M^2}\boldsymbol{\nabla}p - \frac{1}{Re}\boldsymbol{\nabla} \cdot \boldsymbol{\tau}(\boldsymbol{u}) = \boldsymbol{f} \,, \tag{1b}$$

$$\varrho\partial_t \Theta + \varrho\boldsymbol{u} \cdot \boldsymbol{\nabla}\Theta + (\gamma - 1)p\boldsymbol{\nabla} \cdot \boldsymbol{u} - \gamma(\gamma - 1)\frac{M^2}{Re}\,\boldsymbol{\tau}(\boldsymbol{u}) : \boldsymbol{d}(\boldsymbol{u}) - \frac{\gamma}{PrRe}\boldsymbol{\nabla}^2\Theta = h \,, \tag{1c}$$

$$p - \varrho\Theta = 0 \,. \tag{1d}$$

Forcing in the bulk is taken into account through the mass, momentum and heat source terms noted j, $\boldsymbol{f}$, and h in the right-hand side of equations (1). Physically, $\boldsymbol{f}$ (resp. j and h) represents the volumetric momentum rate (resp. volumetric mass and energy rates) applied by the control. Finally, $\boldsymbol{d}(\boldsymbol{u})$ and $\boldsymbol{\tau}(\boldsymbol{u})$ are the strain and stress tensors defined as

$$\boldsymbol{d}(\boldsymbol{u}) = \frac{1}{2}\left(\boldsymbol{\nabla}\boldsymbol{u} + \boldsymbol{\nabla}\boldsymbol{u}^T\right) \,, \qquad \boldsymbol{\tau}(\boldsymbol{u}) = -\frac{2}{3}(\boldsymbol{\nabla} \cdot \boldsymbol{u})\,\boldsymbol{I} + 2\boldsymbol{d}(\boldsymbol{u}) \,. \tag{2}$$

Equations (1) have been made nondimensional using the body diameter D and the upstream quantities W_∞, ϱ_∞, Θ_∞ and p_∞ as respective velocity, density, temperature and pressure scales, and the Reynolds and Mach numbers are defined as

$$Re = \frac{\varrho_\infty D W_\infty}{\mu}, \qquad M = \frac{W_\infty}{\sqrt{\gamma R_g \Theta_\infty}} \,, \tag{3}$$

with R_g the ideal gas constant.

The additional effect of forcing at the wall is taken into account in the boundary conditions. To this end, we define a specific control surface Γ_c that can be any arbitrary part of the body wall Γ_w, on which we impose a velocity $\boldsymbol{u}_w$ and temperature Θ_w modeling a subsonic wall injection:

$$\boldsymbol{u} = \boldsymbol{u}_w, \ \Theta = \Theta_w \ \text{on} \ \Gamma_c \,. \tag{4}$$

We chose here the control surface as the base of the model rocket, as sketched in Figure 1. On all other body walls, we enforce no-slip, adiabatic wall conditions:

$$\boldsymbol{u} = \boldsymbol{0}, \ \partial_n\varrho = \partial_n\Theta = 0 \ \text{on} \ \Gamma_w \backslash \Gamma_c \,, \tag{5}$$

where ∂/∂_n is the derivative normal to the surface, and the density condition in (5) is derived from the perfect gas state equation[30]. Note that condition (4) may not be relevant to the case of a subsonic suction, as the number of degrees of freedom corresponding to subsonic inlet and outlet conditions is not the same.

III.   NUMERICAL METHOD

From now on, all governing equations are written as formal relations between differential operators. System (1) can thus be written as

$$\mathcal{B}(\boldsymbol{q})\partial_t\boldsymbol{q} + \mathcal{M}(\boldsymbol{q},\mathcal{G}) = (j, \boldsymbol{f}, h, 0)^T, \tag{6}$$

where $\mathcal{B}$ and $\mathcal{M}$ are differential operators and $\mathcal{G}$ is a set of relevant control parameters (Reynolds and Mach numbers, angle of attack...) assumed to be constant here, so that the dependence in $\mathcal{G}$ is omitted for clarity. In the following, one must distinguish between the complete form of these operators, defined for the state vector $\boldsymbol{q} = (\varrho, \boldsymbol{u}, \Theta, p)^T$, and the reduced form defined for the state vector $\boldsymbol{q} = (\varrho, \boldsymbol{u}, \Theta)^T$, that can be straightforwardly deduced by replacing the pressure terms by their expression issuing from the perfect gas state equation. The complete form is more suitable to the presentation of the theoretical framework, whereas the reduced form is used in the numerics as it requires smaller computational resources. To ease the reading, we omit voluntarily the difference between both forms, the choice of the relevant one being clear from the context. The complete form of all operators is detailed in Appendix B.
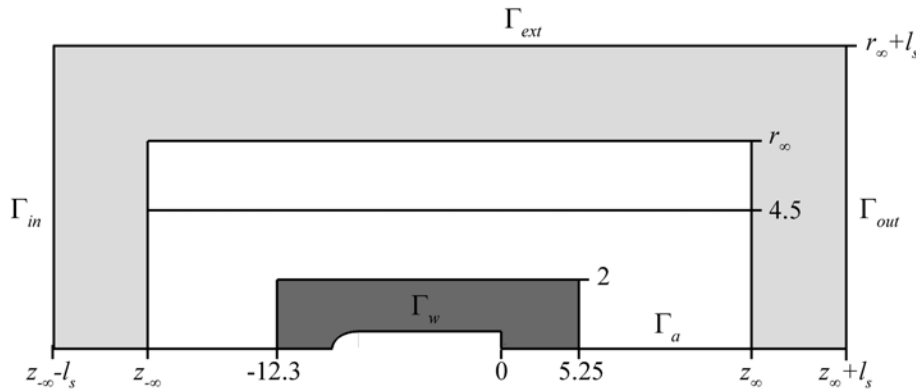

Figure 2: Schematic of the computational domain: the inner solid lines delimit regions characterized by different vertex densities. $z_{-\infty}$, z_{∞} and r_{∞} stand for the dimensions of the inner enclosing cylinder. The inlet, outlet and external boundaries are located at $z = z_{-\infty} - l_s$, $z = z_{\infty} + l_s$ and $r = r_{\infty} + l_s$ respectively, where l_s is the size of the sponge regions used in the numerics, shown as the light grey shaded area. The dark grey shaded area corresponds to the near-wake domain used to normalize the eigenmodes.

The choice of the remaining boundary conditions is crucial in compressible flows. In order to apply appropriate far-field conditions, the body is enclosed into two concentric cylinders defined as

$$r \le r_{\infty} \quad \text{and} \quad z_{-\infty} \le z \le z_{\infty} \qquad \text{(inner cylinder)}, \tag{7a}$$

$$r \le r_{\infty} + l_s \quad \text{and} \quad z_{-\infty} - l_s \le z \le z_{\infty} + l_s \qquad \text{(outer cylinder)}. \tag{7b}$$

The inner enclosing cylinder corresponds to the footprint of the computational domain that would have been used for an incompressible flow, whereas the outer cylinder defines the location of the inlet, outlet and external boundaries (denoted Γ_{in}, Γ_{out} and Γ_{ext} respectively) in the numerics. In the domain enclosed between the cylinders, shown as the light grey shaded area in Figure 2, all fluctuations are progressively damped to negligible levels through artificial dissipation, as the Reynolds number is smoothly decreased from its value defined in (3) to the small value $Re_s = 0.1$ at the boundary of the computational domain. The purpose of such sponge regions is to minimize numerical box size effects by gradually attenuating all vortical and acoustic fluctuations before they reach the boundary of the domain[31]. The Reynolds number in all equations should therefore be replaced by a *computational* Reynolds number $\widetilde{Re}$ defined by $\widetilde{Re}(r, z) = Re$ in the inner cylinder, and

$$\widetilde{Re}(r, z) = Re + (Re_s - Re)\zeta(z, z_{\infty}) \quad \text{if} \quad r \le r_{\infty} \quad \text{and} \quad z > z_{\infty}, \tag{8a}$$

$$\widetilde{Re}(r, z) = Re + (Re_s - Re)\zeta(z, z_{-\infty}) \quad \text{if} \quad r \le r_{\infty} \quad \text{and} \quad z < z_{-\infty}, \tag{8b}$$

$$\widetilde{Re} = \widetilde{Re}(r_{\infty}, z) + (Re_s - \widetilde{Re}(r_{\infty}, z))\zeta(r, r_{\infty}) \quad \text{if} \quad r > r_{\infty}, \tag{8c}$$

where ζ is the function defined by

$$\zeta(a,b) = \frac{1}{2} + \frac{1}{2}\tanh\left\{4\tan\left(-\frac{\pi}{2} + \pi\frac{|a-b|}{l^s}\right)\right\}. \qquad (9)$$

In addition to this artificial damping, numerical dissipation in the sponge zones is increased by progressive grid stretching. The governing equations are then solved using a uniform free-stream flow condition

$$\boldsymbol{u} = (0,0,1)^T, \ \varrho, \Theta = 1 \text{ on } \Gamma_{in} \cup \Gamma_{ext} \cup \Gamma_{out}. \qquad (10)$$

We use the FreeFem++ software [?] to generate a two-dimensional triangulation of the azimuthal plane $\theta = 0$ with the Delaunay–Voronoi algorithm. The mesh refinement is controlled by the vertex densities imposed on both external and internal boundaries. Regions where the mesh density varies are depicted by the solid lines in Figure 1. All equations are numerically solved by a finite-element method using the same mesh, built with $z_{-\infty} = -100$, $z_\infty = 300$, $r_\infty = 25$ and $l_s = 200$, hence resulting in 692606 triangles. A set of equations is first multiplied by r to avoid the singularity on the $r = 0$ axis. The associated variational formulation is then derived and spatially discretized onto a basis of Arnold-Brezzi-Fortin MINI-elements[32], with 4-node P_{1b} elements for the velocity components and 3-node P_1 elements for the density and temperature. The sparse matrices resulting from the projection of these variational formulations onto the basis of finite elements are built with the FreeFem++ software.

IV. GLOBAL STABILITY ANALYSIS

The state vector $\boldsymbol{q}$ is split into $\boldsymbol{q} = \boldsymbol{Q} + \epsilon\boldsymbol{q}'$, with $\boldsymbol{Q} = (\rho, U, 0, W, T, P)^T$ a steady axisymmetric base flow and $\boldsymbol{q}' = (\rho', u', v', w', T', p')^T$ a three-dimensional perturbation of infinitesimal amplitude ϵ. Unless specified otherwise, we consider only steady, axisymmetric forcing terms, now rewritten as J, $\boldsymbol{F}$, H, $\boldsymbol{U}_w$ and T_w for consistency.

A. Base flow computations

The base flow is solution of the steady, axisymmetric form of the nonlinear system (6) reading

$$\mathcal{M}_0(\boldsymbol{Q}) = (J, \boldsymbol{F}, H, 0)^T, \qquad (11)$$

where $\mathcal{M}_0$ is the axisymmetric form of operator $\mathcal{M}$. $\boldsymbol{Q}$ satisfies the same boundary conditions as for the Navier–Stokes equations, along with the additional condition $U = 0$, $\partial_r W = \partial_r \rho = \partial_r T = 0$ on Γ_a, obtained for axisymmetric solutions from mass, momentum and internal energy conservation as $r \to 0$. In particular, the condition on Γ_c reads $\boldsymbol{U} = \boldsymbol{U}_w$ and $T = T_w$. We carry out here the global stability analysis of the *unforced* afterbody flow, for which

$$J = 0, \qquad \boldsymbol{F} = \boldsymbol{0}, \qquad H = 0, \qquad \boldsymbol{U}_w = \boldsymbol{0}, \qquad T_w = 1 + \frac{\gamma-1}{2}M^2, \qquad (12)$$

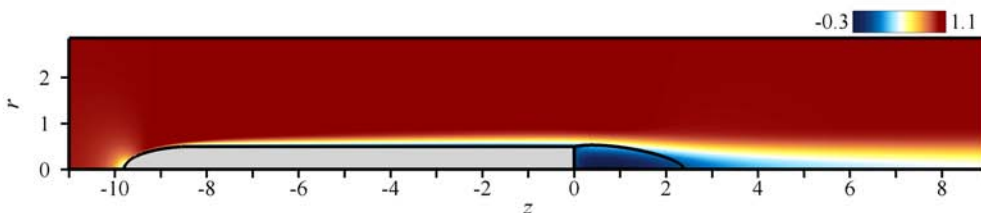i.e. the wall temperature is equal to the free-stream total temperature.

Figure 3: Spatial distribution of streamwise velocity for the steady axisymmetric base flow at $Re = 999$ and $M = 0.5$. The solid line in the flow indicates the separatrix of the recirculation zone.

In the present study, $\boldsymbol{Q}$ is obtained using an iterative Newton method[33] involving successive iterations of a guess value $\bar{\boldsymbol{Q}}$. At each step, a linear problem is solved using the UMFPACK library[?], which consists in a sparse direct LU solver[34,35]. The iterative process is carried out until the $\mathcal{L}^2$-norm of the residual of the governing equations for $\bar{\boldsymbol{Q}}$ becomes smaller than 10^{-12}. In the limit of low Mach numbers, the flow quantities are expanded as power series in γM^2,[36] and the initial guess is obtained by continuation from the incompressible solution computed using the solver presented in Meliga et $al.$[37]. For Mach numbers $M > 0.3$, the initial guess is simply chosen as a solution of the compressible equations computed for a lower value of the Mach number. Since we do not use the governing equations under their conservative form, the numerical method cannot easily account for the presence of shock waves in the computational domain, as this would require to use mesh refinement techniques to fully resolve the viscous structure of the shock. Consequently, the local Mach number $M_l = M\|\boldsymbol{U}\|/\sqrt{T}$ must remain smaller than one everywhere in the flow, and the free stream Mach number can therefore be increased up to $M \sim 0.7$ for the present computations.

The accuracy of the numerical method has been assessed by computing first the flow past a sphere at low Mach numbers $M = 0.1$ and 0.2, and by comparing the drag coefficients and recirculation lengths to the incompressible values documented in the literature[39,40]. The dynamics is from now on exemplified by setting $M = 0.5$. Figure 3 shows contours of the base flow streamwise velocity for $Re = 999$ and $M = 0.5$. The solid line is the streamline linking the separation point to the stagnation point on the $r = 0$ axis, and defines the separatrix delimiting the recirculation bubble behind the base. The classical topology of wake flows is retrieved, with a recirculation region of length $\sim 2.5D$ developing in the wake of the afterbody, and negative values of the streamwise velocity reaching 30% of the free-stream velocity close to the axis.

B.   Eigenvalue computations

All perturbations are sought under the form of normal modes

$$\boldsymbol{q}' = \hat{\boldsymbol{q}}(r,z)e^{(\sigma+\mathrm{i}\omega)t+\mathrm{i}m\theta} + \text{c.c.}\,, \tag{13}$$

where $\hat{\boldsymbol{q}} = (\hat{\rho}, \hat{\boldsymbol{u}}, \hat{T}, \hat{p})^T$ is the so-called global mode and c.c. denotes the complex conjugate of the preceding expression. The azimuthal wavenumber of the global mode is m, its growth rate and pulsation are σ and ω respectively. Substituting $\boldsymbol{q} = \boldsymbol{Q} + \epsilon\boldsymbol{q}'$ into (11) and retaining only terms of order ϵ yields a system of linearized equations governing the normal mode under the form of a generalized eigenvalue problem for $\lambda = \sigma + \mathrm{i}\omega$ and $\hat{\boldsymbol{q}}$:

$$\lambda\mathcal{B}(\boldsymbol{Q})\hat{\boldsymbol{q}} + \mathcal{A}_m(\boldsymbol{Q})\hat{\boldsymbol{q}} = \boldsymbol{0}\,. \tag{14}$$

In (14), $\mathcal{A}_m$ is the complex operator obtained from $\mathcal{A} = \partial\mathcal{M}/\partial\boldsymbol{q}$ by replacing the θ derivatives by $\mathrm{i}m$. The global mode satisfies homogeneous boundary conditions linearized from the Navier–Stokes conditions. For the $m = \pm 1$ modes discussed in the following, we use the additional condition $\hat{w} = \hat{\rho} = \hat{T} = 0$, $\partial_r\hat{u} = \partial_r\hat{v} = 0$ at the axis. Eigenproblem (14) is solved using the "Implicitly Restarted Arnoldi method" of the ARPACK library[?] based upon a shift and invert strategy[41].

To normalize the $m = \pm 1$ global modes, we impose first the phase of the radial velocity to be zero at $r = 0$ and $z = 1$, i.e. $\hat{u}(0,1)$ is real positive. To normalize the mode amplitude, we introduce the near-wake domain Ω_{in} defined arbitrarily as $z \in [-12.3, 5.25]$ and $r < 2$ (shown as the dark grey shaded area in Figure 2) and the inner product $\int_\Omega \hat{\boldsymbol{a}} \cdot \hat{\boldsymbol{b}}\,r\mathrm{d}\Omega$, where $\hat{\boldsymbol{a}}$ and $\hat{\boldsymbol{b}}$ belong to $\mathbb{C}^n$, $\mathrm{d}\Omega$ is the surface element on the computational domain Ω, and $\cdot$ refers to the canonical hermitian scalar product in $\mathbb{C}^n$. The 'energy' defined by the induced norm is then normalized to unity in the near-wake, so that

$$\int_{\Omega_{in}} \hat{\boldsymbol{q}} \cdot \mathcal{B}\hat{\boldsymbol{q}}\,r\mathrm{d}\Omega = 1\,. \tag{15}$$

Note that for compressible flows, the choice of this inner product is convenient for the numerics but is not physically motivated, as the 'energy' in (15) does not represent any meaningful physical quantity, neither the total energy, nor the total enthalpy of the perturbation.

The results of the stability analysis are somehow reminiscent of that documented in the incompressible wake past a sphere and a disk[40]. The axisymmetric base flow is destabilized at $Re_1 = 484.5$ by a first $m = 1$ mode, named mode 1. This mode is stationary (i.e. $\omega = 0$) and its eigenvector
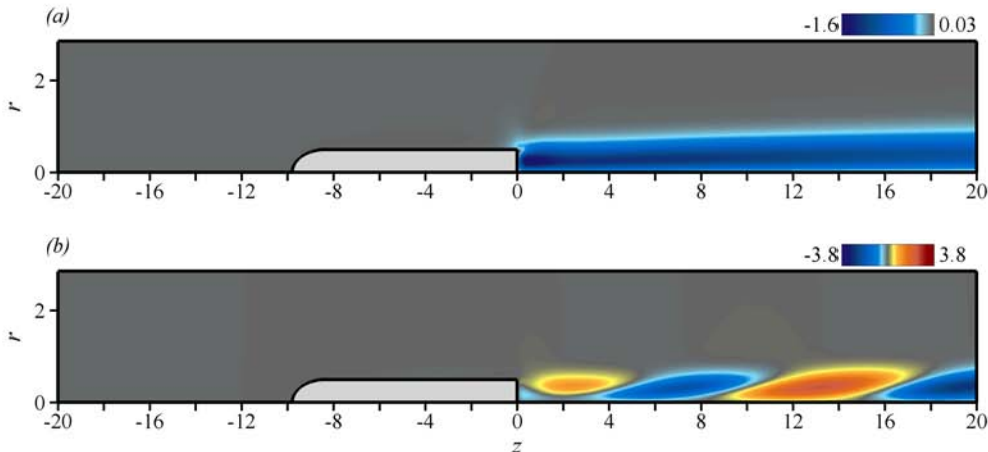
Figure 4: Spatial distribution of streamwise velocity for the three-dimensional disturbances. (a) Stationary mode 1 at the threshold of the first instability - $Re_1 = 484.5$, $M = 0.5$. (b) Oscillating mode 2 at the threshold of the second instability - $Re_2 = 999$, $M = 0.5$ (only the real part is shown). The dark grey hue corresponds to vanishing perturbations.

chosen as $\hat{q}_1 = (\hat{\rho}_1, \hat{u}_1, i\hat{v}_1, \hat{w}_1, \hat{T}_1)^T$ is real using the present normalization. It exhibits streamwise velocity disturbances extending far downstream of the body, as seen from Figure $4(a)$. The azimuthal wavenumber of this mode being $m = 1$, the velocity perturbation is opposite on the other side of the revolution axis, meaning that this mode induces an off-axis displacement of the wake, as in the case of a sphere at zero Mach number[43]. A subsequent instability of the axisymmetric solution occurs at $Re_2 = 999$ for a second $m = 1$ mode, named mode 2. This mode is oscillating with a frequency $\omega_0 = 0.399$ (the associated Strouhal number being $St = \omega_0 D/2\pi U_\infty = 0.063$), and its eigenvector $\hat{q}_2$ is complex. The real part of the streamwise velocity $\hat{w}_2$ shown in Figure $4(b)$ exhibits positive and negative velocity perturbations alternating downstream of the body in a regular, periodic way that defines a local spatial wavelength of about 12 diameters. The imaginary part (not shown here) displays a similar structure, but is approximately in spatial quadrature, its extrema being located close to the nodes of the real part with a small pitch. This mode therefore corresponds to a spiral perturbation rotating in time at the frequency ω_0. Owing to the symmetries of the problem, this mode comes in pair with a second mode being the complex conjugate of the one plotted here, and corresponding to a spiral perturbation rotating in time and winding in space in the opposite direction. In the following, we focus on the oscillating mode 2, which dominates the dynamics of the afterbody flow at larger Reynolds numbers[37,44]. The subscript 2 is thus systematically omitted in order to ease the notation.

V. OPEN-LOOP CONTROL AND SENSITIVITY ANALYSIS TO A STEADY FORCING

We extend here to compressible flows the analyses introduced by Hill[23] and refined by Giannetti & Luchini[25,45], Chomaz[46] and Marquet *et al.*[24] for incompressible flows. In the perspective of open-loop control, we investigate how the stability of the oscillating global mode may be affected by the addition of a small, finite-amplitude forcing in the bulk and at the wall, whose effect is to modify the base flow.

An eigenvalue solution of eigenproblem (14) is explicitly a function of the base flow variables $\lambda = \lambda(\boldsymbol{Q})$, $\boldsymbol{Q}$ itself being a function of the forcing through equations (11). The eigenvalue can therefore be viewed as a function of the forcing $\lambda = \lambda(J, \boldsymbol{F}, H, \boldsymbol{U}_w, T_w)$, and the variation $\delta\lambda$ can be computed with respect to the small variations δJ, $\boldsymbol{\delta F}$, δH, $\boldsymbol{\delta U}_w$ and δT_w, thus defining the *sensitivity analysis to a steady forcing*. In the following, the complex fields $\boldsymbol{\nabla}_J\lambda$, $\boldsymbol{\nabla}_{\boldsymbol{F}}\lambda$ and $\boldsymbol{\nabla}_H\lambda$ denote the sensitivity of the eigenvalue to bulk mass, momentum and energy sources respectively. Similarly, $\boldsymbol{\nabla}_{\boldsymbol{U}_w}\lambda$ and $\boldsymbol{\nabla}_{T_w}\lambda$ denote its sensitivity to a wall velocity and temperature.

The variations are such that

$$\delta\lambda = \int_\Omega \left(\boldsymbol{\nabla}_J\lambda \cdot \delta J + \boldsymbol{\nabla}_{\boldsymbol{F}}\lambda \cdot \boldsymbol{\delta F} + \boldsymbol{\nabla}_H\lambda \cdot \delta H\right) r\mathrm{d}\Omega + \int_{\Gamma_c} \left(\boldsymbol{\nabla}_{\boldsymbol{U}_w}\lambda \cdot \boldsymbol{\delta U}_w + \boldsymbol{\nabla}_{T_w}\lambda \cdot \delta T_w\right) r\mathrm{d}\Gamma, \quad (16)$$

where $d\Gamma$ is the length element along the control surface. The derivation of the sensitivity functions relies on the computation of an adjoint global mode $\hat{q}^\dagger = (\hat{\rho}^\dagger, \hat{u}^\dagger, \hat{T}^\dagger, \hat{p}^\dagger)^T$, i.e. a Lagrange multiplier for the global mode, and of an adjoint base flow $Q^\dagger = (\rho^\dagger, U^\dagger, T^\dagger, P^\dagger)^T$, i.e. a Lagrange multiplier for the base flow. $\hat{q}^\dagger$ and $Q^\dagger$ are herein computed as the solutions of an eigenvalue problem and of a forced linear problem, respectively. Such an approach is classically used in flow control and optimization problems[47,48]. It is worthwhile noting that although the definition of the gradients depends on the choice of the inner product through the computation of the adjoint quantities, the eigenvalue variation computed from (16) does not. All calculations are detailed in Appendix A 2, and we only mention here that the adjoint global modes are normalized with respect to the global modes, so that

$$\int_\Omega \hat{q}^\dagger \cdot \mathcal{B}\hat{q}\, r\, d\Omega = 1\,. \tag{17}$$

This yields the following expressions:

$$(\boldsymbol{\nabla}_J \lambda, \boldsymbol{\nabla}_F \lambda, \boldsymbol{\nabla}_H \lambda) = (\rho^\dagger, U^\dagger, T^\dagger)\,, \quad \boldsymbol{\nabla}_{U_w} \lambda = \rho\rho^\dagger \boldsymbol{n} + \frac{1}{Re}\boldsymbol{\tau}(U^\dagger)\cdot\boldsymbol{n}\,, \quad \boldsymbol{\nabla}_{T_w}\lambda = \frac{\gamma}{PrRe}\boldsymbol{\nabla}T^\dagger \cdot \boldsymbol{n}\,, \tag{18}$$

where $\boldsymbol{n}$ is the outward normal to the control surface oriented from the body to the fluid. Similar functions for the growth rate are obtained by retaining the real parts of these complex fields.

VI. CONTROL IN THE BULK

We use now the formalism presented in Sec. V to appraise how the oscillating mode, taken at the threshold of instability ($Re = 999$ and $M = 0.5$), can be stabilized by forcing in the bulk ($\boldsymbol{\delta U}_w = \boldsymbol{0}$, $\delta T_w = 0$). The sensitivity analysis being linear in essence, the effect of each forcing term (i.e. of each control means) is analyzed individually.

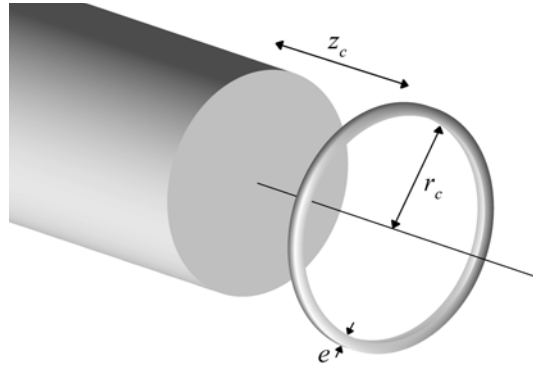### A. Effect of a small control ring

Figure 5: View of a control ring mounted at the rear of the main body, whose action on the base flow is modeled by (19).

We investigate first the effect of momentum forcing in the bulk, for which $\delta J = \delta H = 0$. In practice, such a forcing can be achieved by mounting a small control ring of radius r_c and width e at a distance z_c from the base (Figure 5). We assume that e is small enough for the ring to act as a localized momentum source at the station (r_c, z_c). We also assume that whatever its location, the wake of the device remains steady, meaning that the Reynolds number Re_e based on the width e and the magnitude of the local base flow velocity $\|U\|$ must be small enough. The presence of the ring is not accounted for by any mesh modification, but is modeled by the force it exerts on the flow, an approximation that may be justified through an asymptotic expansion with a viscous inner layer.

As in Hill[23], the force exerted by the ring onto the flow is set opposite to the drag force it experiences. Since the presence of the mode at any arbitrarily small amplitude ϵ creates a modulation of the drag

vector of same amplitude[23,49], one must linearize the total drag vector to compute the force induced by the ring, which can be split into two distinct components

$$\boldsymbol{\delta f} = \boldsymbol{\delta F} + \epsilon \boldsymbol{\delta \hat{f}} \,. \tag{19}$$

$\boldsymbol{\delta F}$ is the steady component of the drag force, which acts by modifying the base flow profiles:

$$\boldsymbol{\delta F}(r,z) = -\frac{1}{2}eC\rho\|\boldsymbol{U}\|\boldsymbol{U}\delta(r - r_c, z - z_c)\,, \tag{20}$$

where C is a drag coefficient depending on Re_e. We use here $e = 0.1$, a value for which the Reynolds number in the recirculating bubble is of order $Re_e \simeq 30$. Consequently, we set $C = 1$, an empirical value determined from the drag coefficient of a cylinder in this range of Reynolds numbers, where it happens to exhibit only very weak variations. $\boldsymbol{\delta \hat{f}}$ is the time-periodic component of the drag force that beats at the same frequency as the global mode. In the quasi-static limit, i.e. assuming that the force follows instantaneously the variation of the flow, it can be written as

$$\boldsymbol{\delta \hat{f}}(r,z) = -\frac{1}{2}e\left[C\rho\|\boldsymbol{U}\|\boldsymbol{\hat{u}} + \left(C\hat{\rho}\|\boldsymbol{U}\| + \left(\frac{C}{\|\boldsymbol{U}\|} + \frac{Re_e}{\|\boldsymbol{U}\|}\frac{\partial C}{\partial Re_e}\right)\rho\boldsymbol{U}\cdot\boldsymbol{\hat{u}}\right)\boldsymbol{U}\right]\delta(r - r_c, z - z_c)\,, \tag{21}$$

where the underlying modification of the drag coefficient $\partial C/\partial Re_e$ is assumed to be zero for simplicity. From a physical point of view, the first term in (21) corresponds to a variation in the direction of the drag vector, whereas the last two terms correspond to a variation in the drag magnitude. If e is small, this force acts as a weak perturbation of the linearized evolution operator under the form of a localized 'force-velocity' coupling, that can also be viewed as a feedback induced by an actuator located at the same station as the sensor[25,45].

The eigenvalue variation induced by the ring can therefore be written as

$$\delta\lambda = \delta_{\boldsymbol{F}}\lambda + \delta_{\boldsymbol{\hat{f}}}\lambda\,. \tag{22}$$

The variation $\delta_{\boldsymbol{F}}\lambda$ owing to the steady force is computed using the sensitivity functions (18), whereas the variation $\delta_{\boldsymbol{\hat{f}}}\lambda$ owing to the feedback force is directly given by projection of the force onto the adjoint global mode. Using the normalization condition (17), we obtain

$$\delta_{\boldsymbol{F}}\lambda = \int_{\Omega} \boldsymbol{U}^{\dagger}\cdot\boldsymbol{\delta F}\,r\mathrm{d}\Omega\,, \qquad \delta_{\boldsymbol{\hat{f}}}\lambda = \int_{\Omega} \boldsymbol{\hat{u}}^{\dagger}\cdot\boldsymbol{\delta\hat{f}}\,r\mathrm{d}\Omega\,, \tag{23}$$

and the corresponding growth rate variations are obtained retaining only the real parts.

Figure 6(b) presents the spatial distribution of the growth rate variation $\delta_{\boldsymbol{F}}\sigma$ arising from the steady drag force. We find both negative and positive variations corresponding respectively to a stabilization and a destabilization of the global mode. The ring has a stabilizing effect when placed along the front part of the separation line, where the shear is maximum. In contrast, it slightly destabilizes the flow if placed on the rear part of the separation line. Figure 6(c) presents the spatial distribution of the variation $\delta_{\boldsymbol{\hat{f}}}\sigma$ induced by the fluctuating feedback force. The ring has a weak stabilizing effect if placed at the internal periphery of the separation line, and a destabilizing effect of same magnitude if placed at the external periphery. In return, the stabilizing effect in Figure 6(a), showing the distribution of the total variation $\delta\sigma = \delta_{\boldsymbol{F}}\sigma + \delta_{\boldsymbol{\hat{f}}}\sigma$, is dominated by the steady component, whereas the contributions of the steady and fluctuating forces add up in the flow region where the ring is destabilizing.

B. Physical interpretation of the stabilizing mechanism in terms of base flow modifications

Since the stabilizing effect can be estimated with a good precision by considering only the contribution of the steady drag force, we propose to further analyze the underlying mechanism by investigating the base flow modification $\boldsymbol{\delta Q}$ induced by the control. Indeed, when the forcing varies, the eigenvalue modification can be interpreted as resulting straightforwardly from the change in the forcing, as has been done in Sec. V, or as resulting from the implicit change in the base flow profiles, as will be done in the following. To this end, we derive here a second sensitivity analysis in which the eigenvalue variation is expressed as a function of $\boldsymbol{\delta Q}$, thus defining the *sensitivity analysis to base flow modifications*, as originally formulated for parallel flows by Bottaro *et al.*[50] and Hwang & Choi[51] and recently generalized to spatially developing flows by Marquet *et al.*[24].
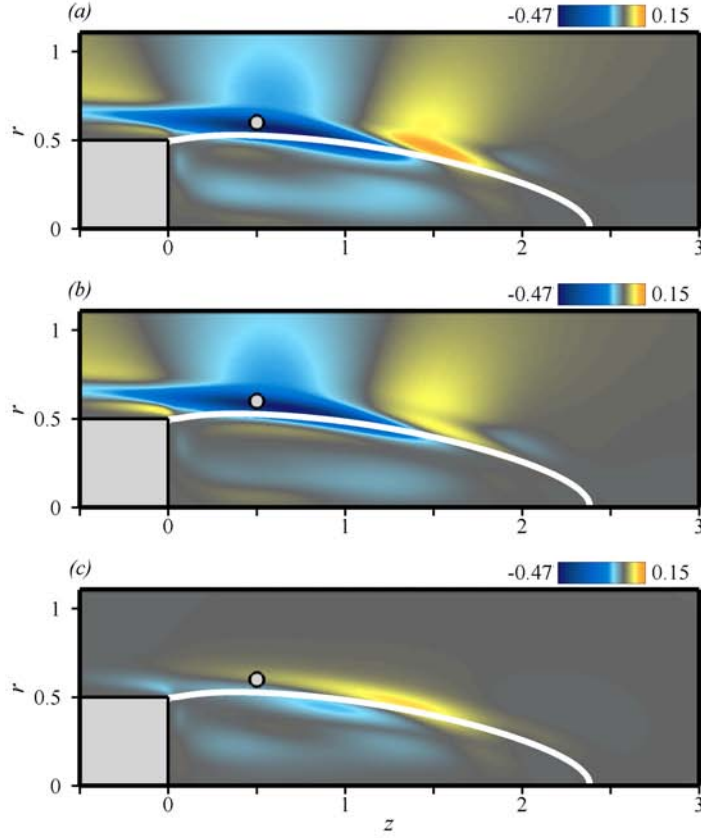
Figure 6: Growth rate variation $\delta\sigma(r_c, z_c)$ owing to the introduction of a small control ring whose presence is modeled by (19), with $e = 0.1$ - $Re = 999$, $M = 0.5$. The total variation in (a) can be decomposed into $\delta\sigma = \delta_{\boldsymbol{F}}\sigma + \delta_{\hat{\boldsymbol{f}}}\sigma$. The variation $\delta_{\boldsymbol{F}}\sigma$ shown in (b) originates from the steady force $\boldsymbol{\delta F}$ modeled by (20) and the variation $\delta_{\hat{\boldsymbol{f}}}\sigma$ shown in (c) results from the feedback force $\boldsymbol{\delta\hat{f}}$ modeled by (21). The color look-up table is identical for all three figures to ease the comparison between results. The circle symbol at $(r_c, z_c) = (0.6, 0.5)$ denotes the position for which we carry out the sensitivity analysis to base flow modifications.

For each specific ring position, the base flow modification $\boldsymbol{\delta Q}$ can be computed explicitly as the solution of the linear problem

$$\mathcal{A}_0\boldsymbol{\delta Q} = (0, \boldsymbol{\delta F}, 0, 0)^T \tag{24}$$

forced by the drag force (20), with homogeneous boundary conditions at the base. Using a Lagrangian formalism similar to that introduced in Sec. V, we introduce now the complex fields $\boldsymbol{\nabla}_\rho\lambda$, $\boldsymbol{\nabla}_{\rho\boldsymbol{U}}\lambda$, $\boldsymbol{\nabla}_{\rho T}\lambda$ and $\boldsymbol{\nabla}_P\lambda$ defining the sensitivity of the eigenvalue to a modification of the base flow density, momentum, internal energy and pressure. We can now compute the eigenvalue variation $\delta\lambda$ as

$$\delta\lambda = \int_\Omega \left(\boldsymbol{\nabla}_\rho\lambda \cdot \delta\rho + \boldsymbol{\nabla}_{\rho\boldsymbol{U}}\lambda \cdot \delta(\rho\boldsymbol{U}) + \boldsymbol{\nabla}_{\rho T}\lambda \cdot \delta(\rho T) + \boldsymbol{\nabla}_P\lambda \cdot \delta P\right) r\mathrm{d}\Omega, \tag{25}$$

the corresponding sensitivities for the growth rate being obtained as above by retaining only the real parts of these complex fields. The sensitivity of the eigenvalue to base flow modifications is defined by the field $\boldsymbol{\nabla}_{\boldsymbol{Q}}\lambda = (\boldsymbol{\nabla}_\rho\lambda, , \boldsymbol{\nabla}_{\rho\boldsymbol{U}}\lambda, \boldsymbol{\nabla}_{\rho T}\lambda, \boldsymbol{\nabla}_P\lambda)^T$, so that

$$\delta\lambda = \int_\Omega \boldsymbol{\nabla}_{\boldsymbol{Q}}\lambda \cdot (\mathcal{H}\boldsymbol{\delta Q}) r\mathrm{d}\Omega. \tag{26}$$

In (26), $\mathcal{H}$ is the matrix mapping from non-conservative onto conservative perturbation quantities, so that $\mathcal{H}\boldsymbol{\delta Q}$ represents the base flow modification recast into conservative variables. All calculations

are detailed in Appendix A 1. Using the normalization condition (17), we obtain

$$(\boldsymbol{\nabla}_\rho\lambda, \boldsymbol{\nabla}_{\rho\boldsymbol{U}}\lambda, \boldsymbol{\nabla}_{\rho T}\lambda, \boldsymbol{\nabla}_P\lambda)^T = -\mathcal{H}^{-1\dagger}\left\{\frac{\partial}{\partial \boldsymbol{Q}}\left(\lambda\mathcal{B}\hat{\boldsymbol{q}} + \mathcal{A}_m\hat{\boldsymbol{q}}\right)\right\}^\dagger \hat{\boldsymbol{q}}^\dagger, \tag{27}$$

where the $\dagger$ superscript denotes the adjoint of the preceding operator.

For a modification $\boldsymbol{\delta Q}$, such an approach allows to compute separately the four integrals

$$\delta_\rho\lambda = \int_\Omega \boldsymbol{\nabla}_\rho\lambda \cdot \delta\rho\, r\mathrm{d}\Omega, \qquad\qquad \delta_{\rho\boldsymbol{U}}\lambda = \int_\Omega \boldsymbol{\nabla}_{\rho\boldsymbol{U}}\lambda \cdot \boldsymbol{\delta}(\rho\boldsymbol{U})\, r\mathrm{d}\Omega,$$

$$\delta_{\rho T}\lambda = \int_\Omega \boldsymbol{\nabla}_{\rho T}\lambda \cdot \delta(\rho T)\, r\mathrm{d}\Omega, \qquad \delta_P\sigma = \int_\Omega \boldsymbol{\nabla}_P\lambda \cdot \delta P\, r\mathrm{d}\Omega, \tag{28}$$

$\delta\lambda$ being then the sum of these four contributions. Physically, $\delta_{\rho\boldsymbol{U}}\sigma$ corresponds to the growth rate variation that would be computed in a fictitious flow for which only the momentum components would be allowed to vary, all other components being kept artificially fixed. If only the contribution of the streamwise component is considered, one retrieves the variation previously investigated in the framework of the local stability of parallel flows[50,51]. It should be kept in mind that for real developing flows such as those considered here, the ring acts by modifying all components of the base flow, meaning that the modifications of density, momentum, internal energy and pressure cannot be prescribed individually but are connected one to another through (24). Such a decomposition is therefore qualitative and used only as a means to gain insight at the mechanisms at work by estimating the importance of each individual base flow component in the stabilizing effect.

It is also possible to interpret the eigenvalue variation in terms of a competition between an *advection mechanism* and a *production mechanism*. In the local theory, this distinction has been formalized via the concepts of convective and absolute instability: the flow is said to be locally convectively unstable if its advection by the base flow dominates over its production, and locally absolutely unstable otherwise. For incompressible flows, Marquet *et al.*[24] have shown that it is straightforward to split the sensitivity function and to identify contributions accounting for the advection and production of disturbances. The case of compressible flows is more involved, as the perturbation may exchange energy with the base flow in different ways. To identify such advection and production terms, we linearize the governing equations, first expressed into integral formulation and conservative variables. The physical origin of all terms in (14) then naturally arises when turning back into non-conservative variables. For instance, the nonlinear term $\varrho\boldsymbol{u}\cdot\boldsymbol{\nabla}\Theta$ in the energy equation (1c) corresponds to the advection of energy by the flow. Its linearization gives rise to two classes of terms in the linearized energy equation:

1. $\hat{\rho}\boldsymbol{U}\cdot\boldsymbol{\nabla}T + \rho\boldsymbol{U}\cdot\boldsymbol{\nabla}\hat{T}$ is an *advection* term associated to the advection of the energy disturbance $\hat{\rho}T + \rho\hat{T}$ by the base flow,

2. $\rho\hat{\boldsymbol{u}}\cdot\boldsymbol{\nabla}T$ is a *production* term associated to the reciprocal advection of the base flow energy ρT by the perturbation.

Consequently, we gather all advection terms into the single advection operator $\mathcal{C}_m$ accounting for the advection of the perturbation (see Appendix B for a detailed expression). All other terms are production terms accounting for the production of disturbances through the advection of the base flow quantities and through the sink/source terms of the governing equations.

It is now possible to split the eigenvalue variation into $\delta\lambda = \delta\lambda_A + \delta\lambda_P$, where $\delta\lambda_A$ is the variation issuing from the change in the advection terms and $\delta\lambda_P$ is the variation issuing from the change in the production terms. Physically, a positive value of $\delta\lambda_A$ indicates a destabilization of the eigenmode owing to a weakening of the disturbances advection. Similarly, a positive value of $\delta\lambda_P$ indicates a destabilization owing to an increase of the disturbances production. These terms are computed respectively as

$$\delta\lambda_A = \int_\Omega \boldsymbol{\nabla}_{\boldsymbol{Q},A}\lambda \cdot \mathcal{H}\boldsymbol{\delta Q}\, r\mathrm{d}\Omega, \qquad \delta\lambda_P = \int_\Omega \boldsymbol{\nabla}_{\boldsymbol{Q},P}\lambda \cdot \mathcal{H}\boldsymbol{\delta Q}\, r\mathrm{d}\Omega, \tag{29}$$

where $\boldsymbol{\nabla}_{\boldsymbol{Q},A}\lambda$ and $\boldsymbol{\nabla}_{\boldsymbol{Q},P}\lambda$ are the advection and production sensitivity functions, computed by isolating the contribution of the advection and production terms to the sensitivity functions (27). We obtain simply

$$\boldsymbol{\nabla}_{\boldsymbol{Q},A}\lambda = -\mathcal{H}^{-1\dagger}\left\{\frac{\partial}{\partial \boldsymbol{Q}}\left(\lambda\mathcal{B}\hat{\boldsymbol{q}} + \mathcal{C}_m\hat{\boldsymbol{q}}\right)\right\}^\dagger \hat{\boldsymbol{q}}^\dagger, \qquad \boldsymbol{\nabla}_{\boldsymbol{Q},P}\lambda = \boldsymbol{\nabla}_{\boldsymbol{Q}}\lambda - \boldsymbol{\nabla}_{\boldsymbol{Q},A}\lambda. \tag{30}$$

Total	$\delta\rho$	$\boldsymbol{\delta(\rho U)}$	$\delta(\rho T)$	δP
-4.2×10^{-1}	3.4×10^{-3}	-4.3×10^{-1}	2.2×10^{-3}	-2.6×10^{-6}

Total	Adv.	Prod.
-4.2×10^{-1}	-3.8×10^{-1}	-4.4×10^{-2}

Table I: Growth rate variation $\delta\sigma$ resulting from the base flow modification induced by a steady drag force, as defined by (20) with $e = 0.1$ - $Re = 999$, $M = 0.5$. This force models the presence of a small control ring at the station $(r_c, z_c) = (0.6, 0.5)$. We also provide the contributions to $\delta\sigma$ arising from the modification of density, momentum, internal energy and pressure, as computed from (28). Results split into the contributions of advection and production, as computed from (29), are provided on the second line.

In order to ease the reading, the mapping matrix $\mathcal{H}$ is from now on omitted and $\boldsymbol{\delta Q}$ stands either for the non-conservative or the conservative form of the base flow modification, unless the choice of the relevant form is not clear from the context.

The analysis is now exemplified by placing the ring at the station $(r_c, z_c) = (0.6, 0.5)$ for which the stabilizing effect achieved is close to the maximum (circle symbol in Figure 6). For this location, the growth rate variation is $\delta\sigma = -4.19 \times 10^{-1}$, a value straightforwardly computed from (23). $\delta\sigma$ can also be computed in two steps, namely by computing first the base flow modification $\boldsymbol{\delta Q}$ from (24), the variation being then retrieved from (25). To this end, the Dirac distribution in (20) is smoothed out in the numerics by a gaussian function of standard deviation $\chi = 1.25 \times 10^{-2}$ centered at (r_c, z_c), which yields $\delta\sigma = -4.23 \times 10^{-1}$. It has been checked that this value varies by less than 1% when decreasing the standard deviation by half, meaning that the chosen gaussian models appropriately a delta function. These values are consistent and validate the present computations since the relative error between the results issuing from both approaches is about 1%. We have carried out decomposition (28): the results are detailed in Table I, where the dominant contribution is systematically displayed in a grey shaded cell, so as to ease the reading. Interestingly, we find that among the four individual variations accounting for the modification of density, momentum, energy and pressure, the momentum variation $\delta_{\rho U}\sigma$ contributes by more than 95% to the total variation $\delta\sigma$. Table I also details the results of decomposition (29), showing that the effect of the advection mechanism dominates over that of production, as $\delta\sigma_A$ represents 90% of the overall variation. This means that a strong increase in the advection of perturbations arising from the modification of the base flow momentum profiles is the leading mechanism involved in the stabilizing effect.

C.   Effect of a heat source localized in the bulk

We set now $\delta J = 0$ and $\boldsymbol{\delta F} = \boldsymbol{0}$, and investigate the growth rate variation resulting from an axisymmetric heat source localized in the bulk, modeled as

$$\delta H(r, z) = \frac{\alpha}{2\pi r_c} \delta(r - r_c, z - z_c), \tag{31}$$

with α the energy rate applied by the control. We chose to heat the flow ($\alpha \geq 0$), so that the control can be viewed as mimicking an axisymmetric gas discharge. We set $\alpha = 10^{-2}$, i.e. the dimensional internal energy rate induced by the control represents 1% of the free-stream internal energy rate based on D, i.e. $\varrho_\infty c_v W_\infty \Theta_\infty D^2$. The growth rate variation is then given by

$$\delta\sigma(r_c, z_c) = \int_\Omega \boldsymbol{\nabla}_H \sigma(r, z) \cdot \delta H(r, z)\, r \mathrm{d}\Omega = \frac{1}{2\pi} \boldsymbol{\nabla}_H \sigma(r_c, z_c)\alpha. \tag{32}$$

Figure 7 presents the spatial distribution of $\delta\sigma$ as given by (32). Heating the base flow has a stabilizing effect for almost all positions in the recirculation region, whereas forcing in the outer region has no effect. Since $\delta\sigma$ is directly proportional to α, the opposite effect would have been obtained by cooling the flow.

In practice, such a forcing can also be achieved by heating the control ring considered in Sec. VI A. The sensitivity analysis being linear in essence, the total growth rate variation achieved by such a technique is simply obtained by adding the individual variations presented in Figures 6(a) and 7,
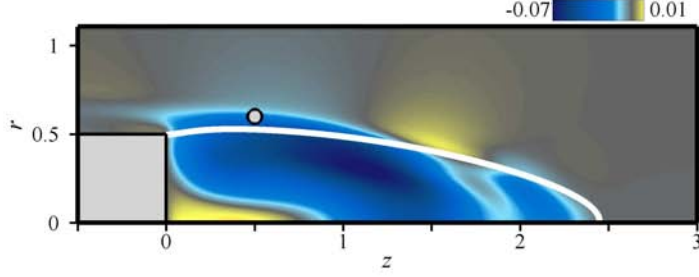
Figure 7: Growth rate variation $\delta\sigma(r_c, z_c)$ induced by a localized heat source modeled by (31) with $\alpha = 10^{-2}$ - $Re = 999$, $M = 0.5$. The circle symbol at $(r_c, z_c) = (0.6, 0.5)$ indicates the position for which the sensitivity analysis to base flow modifications is carried out.

Total	$\delta\rho$	$\boldsymbol{\delta}(\rho\boldsymbol{U})$	$\delta(\rho T)$	δP
-2.0×10^{-2}	1.6×10^{-3}	-2.2×10^{-2}	6.9×10^{-5}	-2.4×10^{-7}

Total	Adv.	Prod.
-2.0×10^{-2}	-1.9×10^{-2}	-1.0×10^{-3}

Table II: Same as Table I, the base flow modification being now induced by a heat source modeled by (31) with $\alpha = 10^{-2}$, localized at the station $(r_c, z_c) = (0.6, 0.5)$ - $Re = 999$, $M = 0.5$.

which yields an increase of the maximum stabilization by 7% (not shown here). Note however that such a comparison is only qualitative, as one can set the relative effects of momentum and heat forcing by modifying either the ring width e or the energy rate α.

The sensitivity analysis to base flow modifications introduced in Sec. VI B can again be used to gain insight at the stabilizing mechanism. The base flow modification is computed by solving equation (24) now forced by the heat source (31), the Dirac distribution being approximated by the same gaussian function already used for the ring computations. For a heat source at $(r_c, z_c) = (0.6, 0.5)$ (circle symbol in Figure 7, located at the same station as the ring in Sec.VI B), we obtain a growth rate variation $\delta\sigma = -1.31 \times 10^{-3}$ as straightforwardly computed from (32) and $\delta\sigma = -1.38 \times 10^{-3}$ as retrieved from the computation of the base flow modification. Decomposition (28) has been carried out and yields results strikingly similar to that found for the control ring (Table II), as we find that the momentum variation $\delta_{\rho U}\sigma$ contributes by more than 90% to the overall variation. Since the modification of the base flow energy component is one order of magnitude larger than that of the momentum components (not shown here), the domination of momentum results from a larger level of sensitivity. The advection/production decomposition (29) has also been carried out, and shows that the effect of the advection mechanism dominates over that of production, as $\delta\sigma_A$ represents 95% of the overall variation. The increase in the disturbances advection resulting from the modification of the momentum profiles is therefore again the dominant mechanism involved in the stabilizing effect.

VII. CONTROL AT THE WALL: APPLICATION TO BASE BLEED

In many practical applications, a localized forcing in the bulk may not be easily tractable, and it is far more convenient to implement only forcing at the wall, obtained in the present framework by setting $\delta J = \delta H = 0$ and $\boldsymbol{\delta F} = \boldsymbol{0}$. We investigate here the effect of wall heating and cooling and of base bleed, i.e. the injection of fluid into the wake by means of a velocity set normal to the wall. This particularizes the analysis to the case of a streamwise velocity $\boldsymbol{\delta U}_w = \delta W_w \boldsymbol{e_z}$, referred to as the bleed velocity. In this case, the eigenvalue variation reads

$$\delta\sigma = \int_{\Gamma_c} \boldsymbol{\nabla}_{W_w}\sigma \cdot \delta W_w \, r\mathrm{d}\Gamma + \int_{\Gamma_c} \boldsymbol{\nabla}_{T_w}\sigma \cdot \delta T_w \, r\mathrm{d}\Gamma, \tag{33}$$

with $\boldsymbol{\nabla}_{W_w}\sigma$ and $\boldsymbol{\nabla}_{T_w}\sigma$ the sensitivity functions obtained from (18) as

$$\boldsymbol{\nabla}_{W_w}\sigma = \rho\rho^\dagger + \frac{1}{Re}\left(-\frac{2}{3}\boldsymbol{\nabla}\cdot\boldsymbol{U}^\dagger + 2\partial_z W^\dagger\right), \qquad \boldsymbol{\nabla}_{T_w}\sigma = \frac{\gamma}{PrRe}\partial_z T^\dagger. \qquad (34)$$

In the incompressible limit ($\rho \to 1$), it can be checked that the wall velocity contribution provided by Hill[23] is retrieved, provided one keeps in mind that our adjoint base flow density $\rho^\dagger$ and the field $P^\dagger$ in Hill's formula play identical roles, as they denote the Lagrange multiplier for the continuity equation. Substituting (34) into (33) allows to distinguish between three distinct contributions associated to mass, viscous and diffusion effects. The first term in the first integral, i.e. the product of the base flow and adjoint base flow densities $\rho\rho^\dagger$ with the bleed velocity δW_w accounts for the effect of the mass flux. The contributions weighted by the inverse of the Reynolds number account for the modification of the viscous friction and of the heat flux owing to diffusion at the wall.

The distributions of the corresponding sensitivity functions are shown at threshold of the instability as the solid lines in Figures 8(a) and 8(b). The sensitivity to the bleed velocity is negative for all radius, thus confirming the stabilizing effect of base bleed early observed by Bearman[13]. The sensitivity is almost constant for $r < 0.3$, and reaches a maximum before the edge, where an actuator imposing a steady blowing should be placed to achieve maximum efficiency. Concerning the sensitivity to a wall temperature, we find positive values at the center decreasing down to negative values at the edge, where the maximum magnitude is reached. To obtain a stabilizing effect, one should thus cool the inner region of the base or heat its periphery. However, the magnitudes of sensitivity are almost two orders of magnitude lower than that to the bleed velocity, meaning that a small-amplitude heating or cooling of the base will have only a limited effect. Confirmation comes from the distributions of the sensitivity functions computed at the supercritical parameter setting $Re = 2000$ and $M = 0.5$, for which the growth rate of the oscillating global mode is $\sigma \simeq 8.2\times10^{-2}$. Results are shown as the dashed lines in Figure 8: the sensitivity to the bleed velocity has significantly increased with the Reynolds number, giving more control authority. On the contrary, the sensitivity to the wall temperature is about the same as for smaller Reynolds numbers, and remains two order of magnitudes lower. In the following, the wall temperature is therefore kept constant and only a uniform bleed velocity is applied at the base.
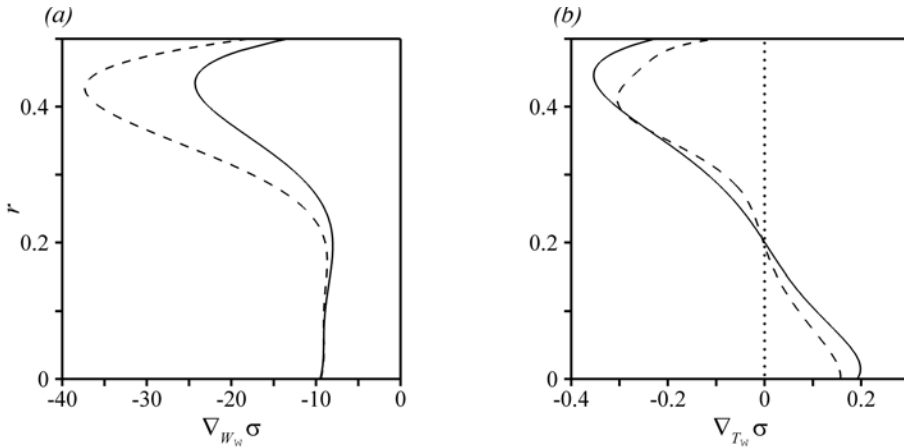

Figure 8: Spatial distribution of the sensitivity to (a) streamwise velocity at the wall $\boldsymbol{\nabla}_{W_w}\sigma$ and (b) wall temperature $\boldsymbol{\nabla}_{T_w}\sigma$ at $M = 0.5$. The solid and dashed lines correspond to the results obtained at $Re = 999$ (i.e. at threshold of the instability) and at $Re = 2000$.

A. Physical interpretation for the stabilizing effect of base bleed

From now on, the Reynolds number is set to $Re = 2000$. We use here a bleed velocity $\delta W_w = 0.01$ representing 1% of the free-stream velocity. The sensitivity analysis to base flow modifications can be again used to gain insight at the stabilizing mechanism. In practice, $\boldsymbol{\delta Q}$ is computed by solving the homogeneous form of equation (24) along with the conditions $\boldsymbol{\delta U} = \delta W_w \boldsymbol{e_z}$ and $\delta T = 0$

Total	$\delta\rho$	$\boldsymbol{\delta}(\rho\boldsymbol{U})$	$\delta(\rho T)$	δP
-3.0×10^{-2}	7.2×10^{-4}	-3.1×10^{-2}	1.7×10^{-4}	2.2×10^{-7}

Total	Adv.	Prod.
-3.0×10^{-2}	-2.1×10^{-2}	-9.5×10^{-3}

Total	$\boldsymbol{\delta}(\rho\boldsymbol{U})_\perp$	$\boldsymbol{\delta}(\rho\boldsymbol{U})_\parallel$
-3.0×10^{-2}	-2.7×10^{-2}	-4.2×10^{-3}

Table III: Same as Table I, the base flow modification being now induced by a uniform bleed velocity $\delta W_w = 0.01$ - $Re = 2000$, $M = 0.5$. The separate contributions of the cross-stream and streamwise momentum components have also been computed and are provided on the third line.

at the base. We obtain $\delta\sigma = -2.96 \times 10^{-2}$ using the sensitivity to a steady forcing and $\delta\sigma = -3.03 \times 10^{-2}$ using the sensitivity to base flow modifications. Decompositions (28) and (29) have been carried out (see Table III for the detailed results). Once again, the stabilizing effect is dominated by the contribution of momentum which represents 98% of the overall variation. The novelty here is that both the modifications of the advection and of the production mechanisms contribute to the stabilization, but the effect of advection still dominates, as $\delta\sigma_A$ represents 70% of the total variation. Base bleed therefore induces simultaneously a strong strengthening of the perturbations advection and a weakening of their production. The contribution owing to the viscous and diffusion terms in (34) represents approximatively 1 % of the overall variation, meaning that the base flow modification owing to the additional mass flux is the leading mechanism involved in the stabilizing effect.
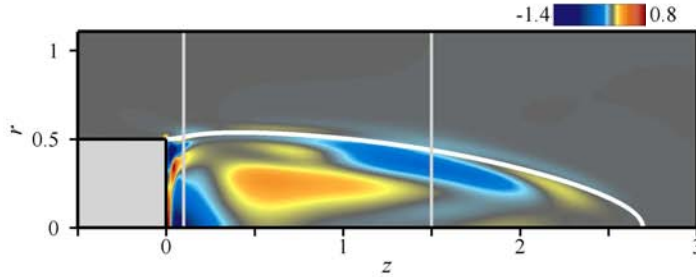

Figure 9: Spatial distribution of the integrand $\boldsymbol{\nabla}_{\boldsymbol{Q},A}\sigma \cdot \mathcal{H}\boldsymbol{\delta Q}(r,z)$. The integration over space of this field yields the variation $\delta\sigma_A$ that dominates the overall growth rate variation - $Re = 2000$, $M = 0.5$, $\delta W_w = 0.01$. The vertical lines at $z = 0.1$ and $z = 1.5$ correspond to the stations for which the base flow momentum profiles are presented in Figures 10 and 11.

Figure 9 presents the spatial distribution of the advection momentum integrand $\boldsymbol{\nabla}_{\boldsymbol{Q},A}\sigma \cdot \mathcal{H}\boldsymbol{\delta Q}(r,z)$, whose integration over space yields the variation $\delta\sigma_A$ that dominates the overall growth rate variation. At a given station, a positive (resp. negative) value indicates that the base flow modification $\boldsymbol{\delta Q}$ induces a destabilization (resp. stabilization) of the global mode. Several stabilizing and destabilizing regions are visible in Figure 9, thus outlining the complex effect of base bleed. For instance, the vicinity of the base and the separation line contribute to a strong stabilization of the global mode, whereas the core of the recirculation contributes to its destabilization. Figure 10 shows the streamwise and cross-stream momentum distributions at the streamwise station $z = 0.1$, i.e. in the core of the upstream stabilizing region located close to the base (leftmost vertical line in Figure 9). The solid and dashed lines refer respectively to the base flow $\boldsymbol{Q}$ and the modified base flow $\boldsymbol{Q} + \boldsymbol{\delta Q}$, whereas the dash-dotted line stands for the corresponding base flow modification $\boldsymbol{\delta Q}$. The grey shaded area evidences the position of the shear-layer region, its center being located at the cross-stream position of maximum shear and its width being equal to the vorticity thickness δ computed from the streamwise momentum profile. The base flow modification is concentrated at the centerline and in the shear-layer region. Owing to the positive values of $\delta(\rho W)$ at the centerline, blowing
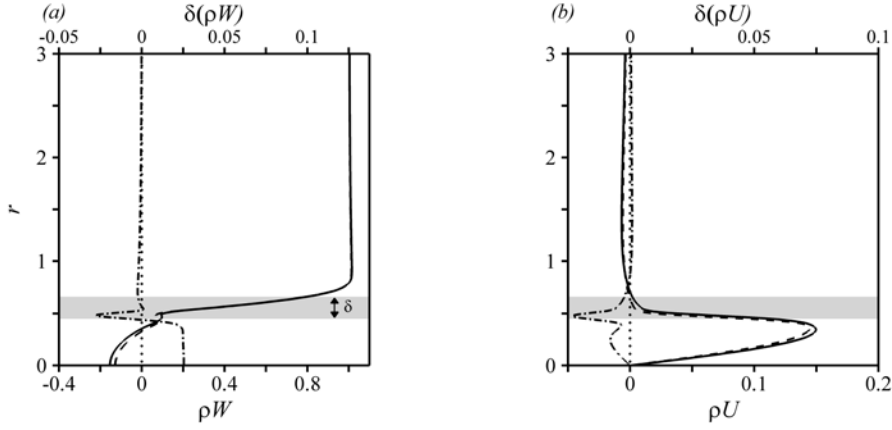
Figure 10: Effect of a bleed velocity $\delta W_w = 0.01$ on the base flow momentum profiles at the streamwise station $z = 0.1$. Spatial distribution of the (a) streamwise momentum ρW and (b) cross-stream momentum ρU. The solid and dashed lines stand for the base flow and the modified base flow, respectively, whereas the dash-dotted lines stand for the corresponding base flow modification. The grey shaded areas evidence the location of the shear-layer region, with δ the vorticity thickness computed from the streamwise momentum profile. The vertical dotted line marks the zero value. $Re = 2000$ - $M = 0.5$.
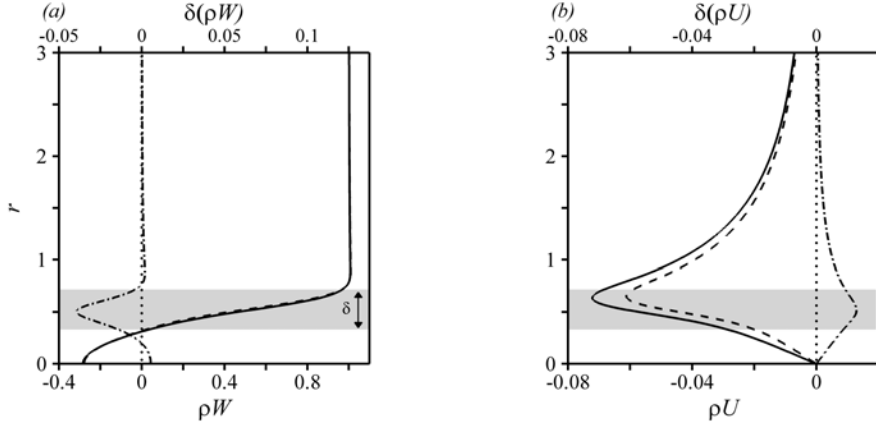

Figure 11: Same as Figure 10 for the streamwise station $z = 1.5$.

reduces the streamwise backflow velocity by approximatively 18 %, whereas the effect on the cross-stream component is somehow subtle. Figure 11 shows similar momentum distributions at the station $z = 1.5$, i.e. in the core of the downstream stabilizing region (rightmost vertical line in Figure 9). The base flow modification is now concentrated in the only shear-layer region, so that the effect of blowing on the streamwise component is barely visible. In contrast, it significantly spreads out the cross-stream momentum gradients over a large cross-stream distance. The stabilizing effect of base bleed is therefore twofold. Close to the base, it increases the streamwise advection, which results in a reduction of the counterflow rate. Further downstream, it increases the cross-stream advection, which tends to reduce the momentum gradients. We have computed the separate contributions of the cross-stream and streamwise momentum components to the variation $\delta_{\rho U}\sigma$. It is worthwhile recalling here that the bleed velocity modifies all components of the base flow, and that the individual contribution of density, momentum, energy and pressure cannot be prescribed arbitrarily. Still, the present decomposition stands as an attempt to compare our interpretations to those previously derived in the framework of the local stability theory, in which one captures only the modification of streamwise momentum, all other components of the base flow being kept artificially constant. The results provided in Table III show that base bleed stabilizes the flow mainly through cross-stream advection, the contribution of streamwise advection to the overall variation $\delta\sigma$ being smaller by one order of magnitude. This questions the usual interpretations based on the local stability theory, stating that base bleed stabilizes the flow by increasing the streamwise advection and by so, increasing the convective nature of the

local instability, as discussed in Sevilla & Martínez-Bazàn[29]. The present results strongly suggest that the action of base bleed is non-parallel in essence, and may not be fully captured nor interpreted by performing only local analyses, at least in the range of Reynolds numbers prevailing in the present study.

B.   Discussion: impact of base flow nonlinearities

It should be kept in mind that the sensitivity analysis is linear and assumes that the departure of Q_w from the unforced base flow Q is finite but weak. To appraise the effect of base flow nonlinearities on the present problem, we investigate now the *nonlinearly forced* base flow Q_w, obtained by solving directly the homogeneous form of the nonlinear base flow equations (11) with the additional condition $U = \delta W_w e_z$ at the base. We present on Figure 12 streamwise velocity contours of the forced base flow Q_w computed for different magnitudes of the bleed velocity ranging from $\delta W_w = 0.001$ to 0.06. Increasing the bleed velocity shifts downstream the recirculating bubble, which is delimited by the streamline linking the leading and trailing stagnation points (evidenced as the solid line). Simultaneously, the recirculating length, defined as the distance between both stagnation points, increases from $2.7D$ at $\delta W_w = 0.001$ to $3.9D$ at $\delta W_w = 0.06$, whereas the backflow velocity significantly decreases from 37% to only 17%.
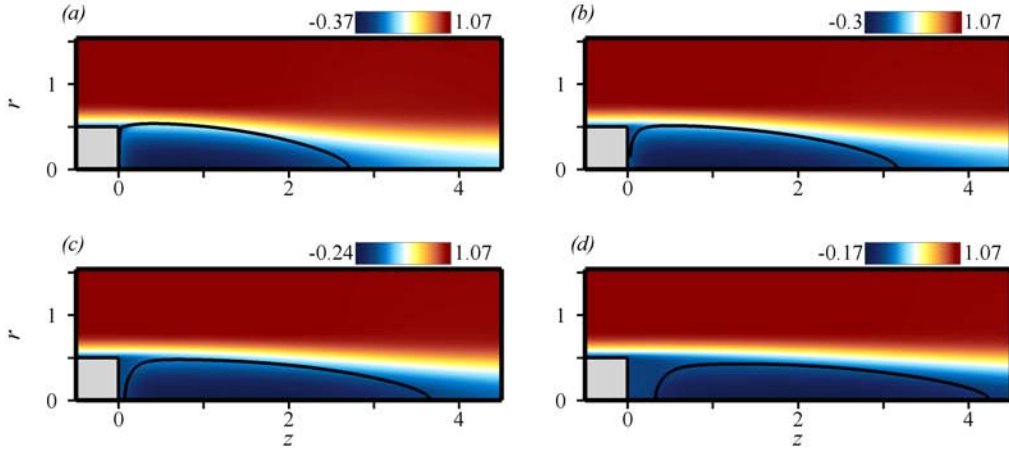

Figure 12: Spatial distribution of streamwise velocity for the nonlinearly forced base flow Q_w, obtained by solving directly the homogeneous form of the nonlinear base flow equations (11) along with the additional condition $U = \delta W_w$ at the base - $Re = 2000$, $M = 0.5$. (a) $\delta W_w = 0.001$, (b) $\delta W_w = 0.02$, (c) $\delta W_w = 0.04$, and (d) $\delta W_w = 0.06$.

The growth rate of the oscillating global mode, directly computed by carrying out the stability analysis of the base flows presented in Figure 12, is shown in Figure 13(a) as a function of δW_w (grey circle symbols), or alternatively as a function of the bleed flow rate δD through the base, defined as

$$\delta D = 8 \int_{\Gamma_c} \rho \delta W_w \, r \mathrm{d}r \,. \tag{35}$$

The growth rate decreases as the bleed velocity increases, confirming the stabilizing effect of base bleed. The solid line corresponds to the evaluation of σ assuming δW_w is small enough for the linear approximation to hold, i.e.

$$\sigma(\delta W_w) = \sigma(\delta W_w = 0) + \int_{\Gamma_c} \boldsymbol{\nabla}_{W_w} \sigma \cdot \delta W_w \, r \mathrm{d}\Gamma \,. \tag{36}$$

The agreement between both approaches is excellent in the range $\delta W_w \leq 0.01$, the difference between linear sensitivity predictions and direct stability computations being not even measurable for $\delta W_w \leq 0.001$. For larger bleed velocities, we observe small discrepancies, as nonlinearities set in. We observe in particular that the decrease in the growth rate computed by the sensitivity analysis
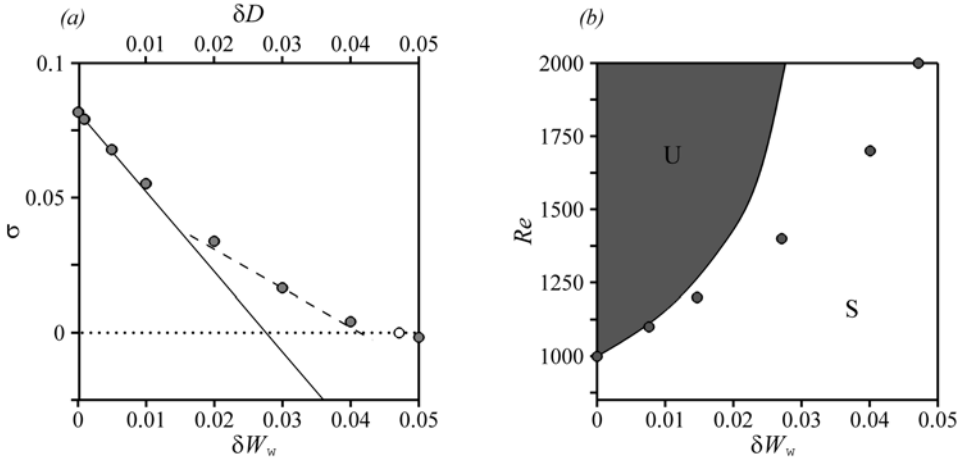
Figure 13: Comparison of the linear results obtained from the sensitivity analysis (solid line) with the nonlinear results obtained from the direct stability analysis of the forced base flow (circle symbols) - M=0.5. (a) Growth rate σ as a function of the bleed velocity δW_w/bleed flow rate δD, at $Re = 2000$. The dashed line stands for the linear results obtained applying the sensitivity analysis to the forced base flow computed for $\delta W_w = 0.03$. (b) Boundary separating the unstable domain (U-labeled shaded area) from the stable domain (S-labeled area) in the ($\delta W_w, Re$)-plane.

slightly overestimates the stabilizing effect of forcing, which turns out to be limited by the nonlinear modifications of the base flow. The critical wall velocity for which the zero-growth rate is achieved is shifted from $\delta W_w \simeq 0.028$ ($\delta D \simeq 0.026$), which stands for the value predicted by the sensitivity analysis, to $\delta W_w \simeq 0.047$, as predicted by direct stability calculations (white circle symbol). However, the difference between both sets of results remains small up to $\delta W_w \simeq 0.02$, indicating that the sensitivity approach is valid even for non-small bleed flow rates close to the one needed to stabilize the flow. Figure 13(b), presents the critical bleed velocity computed as a function of the Reynolds number. The values issuing from the sensitivity analysis (solid line) have been obtained simply by canceling the linear growth rate defined by (36). The values issuing from the direct stability analysis of the forced base flow are also reported as the grey circle symbols. The critical bleed velocity increases monotonically with the Reynolds number, and the sensitivity analysis systematically overestimates the stabilizing effect of the forcing. Still, the magnitude of the bleed velocity necessary to stabilize the flow is predicted reasonably well up to Reynolds numbers $Re \leq 1200$, the agreement being only in order of magnitude afterwards.
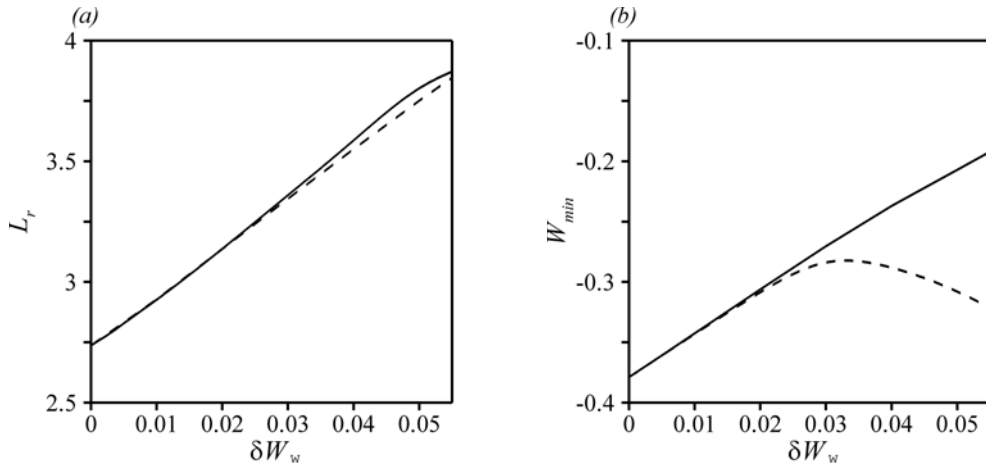

Figure 14: (a) Recirculation length and (b) backflow velocity computed as functions of the bleed velocity. The solid and dashed lines refer to the forced base flow $\boldsymbol{Q}_w$ and to its linear approximation $\boldsymbol{Q} + \delta\boldsymbol{Q}$, respectively - $Re = 2000$, $M = 0.5$.

We present in Figures 14(a) and 14(b) the recirculating length L_r and the backflow velocity computed for different values of the bleed velocity. The solid lines (resp. the dashed lines) correspond to the forced base flow $\mathbf{Q}_w$ (resp. the linear approximation $\mathbf{Q} + \boldsymbol{\delta Q}$). The recirculating length is well predicted, although slightly underestimated, by the linear sensitivity approach, the maximum difference being of order 1 %. The agreement on the backflow velocity is remarkable up to $\delta W_w = 0.03$, a value after which the solution $\mathbf{Q}_w$ departs strongly from its linear estimation. In return, the linear approach fails to reproduce the significant reduction of the backflow velocity discussed previously. This limit value of δW_w corresponds approximately to the one above which the stabilization by base bleed starts being badly estimated by the linear sensitivity approach (Figure 13(b)).

C. Effect of the bleed velocity profile

The present sensitivity formalism can be extended and used to derive optimal control strategies. Such an extension is out of the scope of this study. Still, we aim now, as a simple illustration, at optimizing the stabilization of the oscillating global mode by varying the bleed velocity profiles. Figure 15(b) shows the evolution of the growth rate computed for three different bleed velocity distributions, all results being displayed as functions of the bleed flow rate δD to allow comparison. The solid line corresponds to the uniform distribution investigated in Sec. VII A. The dashed line corresponds to a roughly optimized piecewise-constant distribution depicted in the upper part of Figure 15(a), with low velocity blowing in the center region ($r < 0.3$), i.e. in the region where the sensitivity is the lowest according to Figure 8(a), and high velocity blowing close to the edge, of magnitude twice that at the centerline. The dash-dotted line corresponds to the realistic gaussian jet profile depicted in the lower part of Figure 15(a), whose standard deviation represents 4% of the base diameter and whose center is located at $r = 0.4$, i.e. close to the region of maximum sensitivity. A stronger stabilization is achieved using the optimized bleed distributions, as the critical flow rate drops by approximately 10 % using the piecewise-constant distribution (from $\delta D \simeq 0.026$ to 0.023), and by more than 30% using the gaussian jet profile (down to 0.018), thus illustrating the importance of using physically motivated bleed distributions.
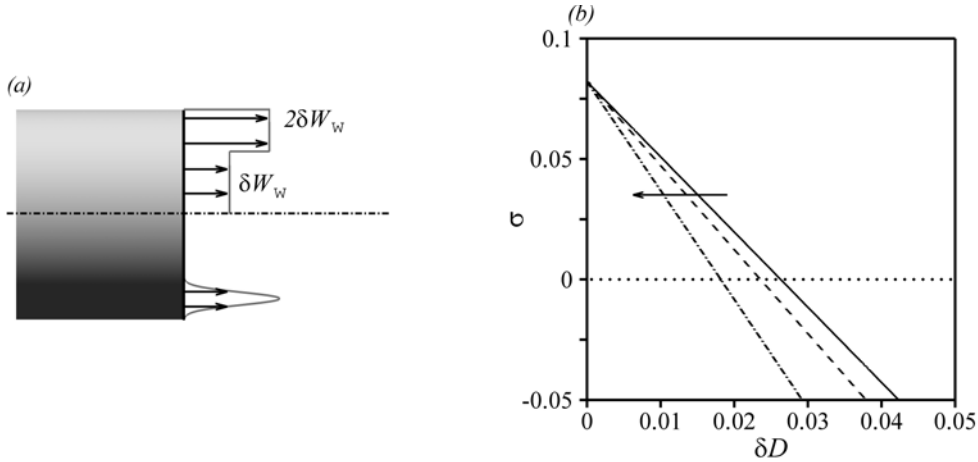

Figure 15: (a) Piecewise-constant distribution and gaussian jet profile used to optimize the stabilization of the oscillating global mode. (b) Growth rate σ as a function of the bleed flow rate δD. Comparison of the linear results obtained from the sensitivity analysis with a uniform velocity distribution (solid line), the piecewise-constant velocity distribution sketched in the upper part of (a) (dashed line), and the gaussian jet profile shown in the lower part of (a) (dash-dotted line) - $Re = 2000$, $M = 0.5$.

From this result, one can imagine a more powerful nonlinear control algorithm based on a steepest descent technique, in which one would apply recursively the computation carried out above, and would converge to an optimal bleed distribution minimizing the growth rate by defining at each step a new forcing descending in the direction of the negative gradient. Considering for simplicity the case of uniform bleed, such an algorithm would consist in moving along the curve linking the grey circles in Figure 13(b). At each point, the present sensitivity analysis provides with an accurate estimation of the sensitivity with respect to a modification of the bleed velocity. For instance, the dashed line

in Figure 13(a) stands for the values of σ obtained by applying the sensitivity analysis no more to the unforced base flow, but to the forced base flow $\boldsymbol{Q}_w$ computed for $\delta W_w = 0.03$. We obtain a good estimation of the actual growth rate obtained when varying the base bleed intensity around this specific value. This formalism therefore stands as a promising tool for the design of future control strategies, even at realistic parameter settings were nonlinear effects may be important.

VIII.   CONCLUSION

The global stability of a compressible afterbody flow has been investigated in the high subsonic regime. The base flow and stability equations have been derived and numerically solved. The resulting bifurcation sequence is the same as for incompressible axisymmetric wakes, with a first instability occurring for a stationary global mode of azimuthal wavenumber $m = 1$, and a second instability occurring for an oscillating global mode of same azimuthal wavenumber. Following Hill[23], a theoretical framework for the control of unstable global modes has been developed. It stands for a systematic approach of open-loop control, in which gradients, also named sensitivity functions, are used to predict beforehand the eigenvalue variation induced by a steady forcing in the bulk or at the wall. This variation can be investigated as a function of the forcing itself, or as a function of the base flow modification induced by the forcing. In both cases, the analytical expression of the sensitivity functions has been derived using adjoint methods.

This formalism has been applied to the oscillating global mode. We have studied the ability of various open-loop control techniques to stabilize this mode as a possible way to alleviate afterbody flow unsteadiness. The global mode is most sensitive to bulk forcing within the recirculating bubble. Momentum forcing may be achieved in practice by introducing a small ring in the lee of the afterbody. When sufficiently small, the control ring is modeled by the force it exerts on the flow, which is the opposite of the pure drag force it experiences. Since the drag vector at the location of the ring is modulated by the momentum perturbation, the effect of such a control device is twofold: it modifies the eigenvalue both by modifying the steady base flow and by introducing a feedback on the perturbation. Both contributions are of the same order, but for the present case, the effect of the base flow modification dominates over that of the feedback. We have shown that the efficiency of the control can be improved by heating the ring, which then acts as an additional heat source. Mass injection at the wall has a stabilizing effect if fluid is blown through the whole base (a method termed base bleed), the sensitivity of the global mode being dominated by the effect of the additional mass flux. Physical interpretations have been proposed for the observed stabilizing effects, that rely on the identification of advection and production terms. The proposed decomposition shows that, for all techniques considered, the stabilization is due to a strengthening in the downstream advection of disturbances.

The present approach can be easily applied to other compressible flow configurations, as for instance cavity flows or hot jets that are known to sustain global instabilities. Extending the present approach to the case of transonic and supersonic flows, where one must deal with the presence of shock waves in the flow, also deserves future efforts, for instance it may open new ways to explore the problem of the shock-induced transonic-buffet onset on airplanes[30].

Appendix A: DERIVATION OF THE SENSITIVITY FUNCTIONS

We use from now on the compact notation

$$\left\langle \hat{\boldsymbol{a}}, \hat{\boldsymbol{b}} \right\rangle = \int_\Omega \hat{\boldsymbol{a}} \cdot \hat{\boldsymbol{b}}\, r \mathrm{d}\Omega, \qquad \left\langle\!\left\langle \hat{\boldsymbol{a}}, \hat{\boldsymbol{b}} \right\rangle\!\right\rangle = \int_{\Gamma_c} \hat{\boldsymbol{a}} \cdot \hat{\boldsymbol{b}}\, r \mathrm{d}\Gamma. \tag{A1}$$

1. Sensitivity to base flow modifications

The eigenvalue variation $\delta\lambda$ and the base flow modification $\boldsymbol{\delta Q}$ are such that

$$\delta\lambda = \delta\sigma + \mathrm{i}\delta\omega = \left\langle \boldsymbol{\nabla_Q}\lambda\,,\,\boldsymbol{\delta Q} \right\rangle. \tag{A2}$$

In the present formalism, the base flow $\boldsymbol{Q}$ is the *control variable*, the eigenpair $\{\hat{\boldsymbol{q}}, \lambda\}$ is the *state variable* and eigenproblem (14) is the *state equation*, i.e. the constraint to be satisfied. We introduce a Lagrange multiplier $\hat{\boldsymbol{q}}^\dagger$ (also known as *adjoint* or *co-state* variable) for the state variable, now referred to as the adjoint perturbation, and define the functional

$$\mathcal{L}(\boldsymbol{Q}, \hat{\boldsymbol{q}}^\dagger, \hat{\boldsymbol{q}}, \lambda) = \lambda - \left\langle \hat{\boldsymbol{q}}^\dagger\,,\,\lambda\mathcal{B}(\boldsymbol{Q})\hat{\boldsymbol{q}} + \mathcal{A}_m(\boldsymbol{Q})\hat{\boldsymbol{q}} \right\rangle. \tag{A3}$$

The gradient with respect to any variable s is defined as

$$\frac{\partial\mathcal{L}}{\partial s}\delta s = \lim_{\epsilon\to 0}\frac{\mathcal{L}(s + \epsilon\delta s) - \mathcal{L}(s)}{\epsilon}. \tag{A4}$$

We assume that the state equation is satisfied for any arbitrary base flow modification, so that the gradient of the functional with respect to the adjoint variable is zero. It can be checked that the gradient with respect to the state variable is zero, provided we define $\hat{\boldsymbol{q}}^\dagger$ as the solution of the adjoint eigenvalue problem

$$\lambda^*\mathcal{B}^\dagger\left(\boldsymbol{Q}\right)\hat{\boldsymbol{q}}^\dagger + \mathcal{A}_m^\dagger\left(\boldsymbol{Q}\right)\hat{\boldsymbol{q}}^\dagger = \boldsymbol{0}, \tag{A5}$$

along with the normalization condition (17). In $(A5)$, $\mathcal{B}^\dagger$ and $\mathcal{A}_m^\dagger$ are the adjoint of operators $\mathcal{B}$ and $\mathcal{A}_m$, obtained by integrating by parts the disturbance equations[52]. The boundary conditions to be fulfilled by the adjoint perturbations are such that all boundary terms arising during the integration by part vanish, which imposes conditions identical to that of the global modes. The eigenvalue variation now reads

$$\delta\lambda = \frac{\partial\mathcal{L}}{\partial\boldsymbol{Q}}\boldsymbol{\delta Q}. \tag{A6}$$

The gradient of the functional with respect to the base flow can be expressed as

$$\frac{\partial\mathcal{L}}{\partial\boldsymbol{Q}}\boldsymbol{\delta Q} = -\left\langle \hat{\boldsymbol{q}}^\dagger\,,\,\frac{\partial}{\partial\boldsymbol{Q}}\Big(\lambda\mathcal{B}(\boldsymbol{Q})\hat{\boldsymbol{q}} + \mathcal{A}_m(\boldsymbol{Q})\hat{\boldsymbol{q}}\Big)\boldsymbol{\delta Q} \right\rangle = -\left\langle \left\{\frac{\partial}{\partial\boldsymbol{Q}}\Big(\lambda\mathcal{B}(\boldsymbol{Q})\hat{\boldsymbol{q}} + \mathcal{A}_m(\boldsymbol{Q})\hat{\boldsymbol{q}}\Big)\right\}^\dagger\hat{\boldsymbol{q}}^\dagger\,,\,\boldsymbol{\delta Q} \right\rangle, \tag{A7}$$

so that the sensitivity function $\boldsymbol{\nabla_Q}\lambda$ is given by

$$\boldsymbol{\nabla_Q}\lambda = -\left\{\frac{\partial}{\partial\boldsymbol{Q}}\Big(\lambda\mathcal{B}(\boldsymbol{Q})\hat{\boldsymbol{q}} + \mathcal{A}_m(\boldsymbol{Q})\hat{\boldsymbol{q}}\Big)\right\}^\dagger\hat{\boldsymbol{q}}^\dagger. \tag{A8}$$

Because we use non-conservative variables in the numerics, expression $(A8)$ corresponds to the sensitivity function $\boldsymbol{\nabla_Q}\lambda = (\boldsymbol{\nabla_\rho}\lambda,, \boldsymbol{\nabla_U}\lambda, \boldsymbol{\nabla_T}\lambda, \boldsymbol{\nabla_P}\lambda)^T$, where $\boldsymbol{\nabla_\rho}\lambda$, $\boldsymbol{\nabla_U}\lambda$, $\boldsymbol{\nabla_T}\lambda$ and $\boldsymbol{\nabla_P}\lambda$ define the sensitivity of the eigenvalue to a small modification of the base flow density, velocity, temperature and pressure, such that

$$\delta\lambda = \int_\Omega \left(\boldsymbol{\nabla_\rho}\lambda\cdot\delta\rho + \boldsymbol{\nabla_U}\lambda\cdot\boldsymbol{\delta U}\right) + \boldsymbol{\nabla_T}\lambda\cdot\delta T + \boldsymbol{\nabla_P}\lambda\cdot\delta P\right) r\mathrm{d}\Omega. \tag{A9}$$

To derive the sensitivity functions in term of the conservative variables, as defined by (27), we simply substitute $\boldsymbol{\delta Q}$ by its conservative counterpart $\mathcal{H}\boldsymbol{\delta Q}$ into $(A7)$, since both relations $(25) - (A9)$ are to be simultaneously satisfied.

In closing this section, it should be noted that such an approach is very similar to that used in optimization problems, where one enforces the stationary of a Lagrangian as a means to minimize a given functional under specific constraint. We would like to insist that no such stationarity is enforced here, and that the functional is only used as a means to compute the different gradients of interest.

2. Sensitivity to a steady forcing

The base flow $\boldsymbol{Q}$ and the eigenpair $\{\lambda, \hat{\boldsymbol{q}}\}$ solution of the state equations $(11) - (14)$ are now the state variables, and the forcing terms $\mathscr{F} = \{J, \boldsymbol{F}, H, \boldsymbol{U}_w, T_w\}$ are the control variables. In addition to the adjoint perturbation $\hat{\boldsymbol{q}}^\dagger$, we introduce a Lagrange multiplier for the base flow $\boldsymbol{Q}^\dagger$, referred to as the adjoint base flow, and Lagrange multipliers $\boldsymbol{U}_w^\dagger$ and $T_w^\dagger$ for the wall velocity and temperature at the base. We define a new functional as

$$
\mathscr{L}(\mathscr{I}, \boldsymbol{Q}^\dagger, \boldsymbol{Q}, \hat{\boldsymbol{q}}^\dagger, \hat{\boldsymbol{q}}, \lambda) = \lambda - \left\langle \hat{\boldsymbol{q}}^\dagger, \lambda \mathcal{B}(\boldsymbol{Q})\hat{\boldsymbol{q}} + \mathcal{A}_m(\boldsymbol{Q})\hat{\boldsymbol{q}} \right\rangle - \left\langle \boldsymbol{Q}^\dagger, \mathcal{M}_0(\boldsymbol{Q}) - (J, \boldsymbol{F}, H, 0)^T \right\rangle
$$
$$
- \left\langle\!\left\langle \boldsymbol{U}_w^\dagger, \boldsymbol{U} - \boldsymbol{U}_w \right\rangle\!\right\rangle - \left\langle\!\left\langle T_w^\dagger, T - T_w \right\rangle\!\right\rangle . \tag{A10}
$$

As in appendix A 1, we assume that the state equations are satisfied for any modification, and that the adjoint perturbation is solution of eigenproblem $(A5)$ along with the normalization condition (17). This yields

$$
\delta\lambda = \left(\frac{\partial \mathscr{L}}{\partial \mathscr{F}} + \frac{\partial \mathscr{L}}{\partial \boldsymbol{Q}} \frac{\partial \boldsymbol{Q}}{\partial \mathscr{F}} \right) \delta \mathscr{F} . \tag{A11}
$$

If we enforce that the gradient of the functional with respect to the base flow $\boldsymbol{Q}$ is zero, as will be discussed in the following, $(A11)$ can be rewritten as

$$
\delta\lambda = \frac{\partial \mathscr{L}}{\partial \mathscr{F}} \delta \mathscr{F} = \frac{\partial \mathscr{L}}{\partial J}\delta J + \frac{\partial \mathscr{L}}{\partial \boldsymbol{F}}\boldsymbol{\delta F} + \frac{\partial \mathscr{L}}{\partial H}\delta H + \frac{\partial \mathscr{L}}{\partial \boldsymbol{U}_w}\boldsymbol{\delta U}_w + \frac{\partial \mathscr{L}}{\partial T_w}\delta T_w , \tag{A12}
$$

and the sensitivity functions can be expressed from the gradients of the functional according to

$$
\frac{\partial \mathscr{L}}{\partial J}\delta J = \left\langle \boldsymbol{\nabla}_J \lambda, \delta J \right\rangle, \qquad \frac{\partial \mathscr{L}}{\partial \boldsymbol{F}}\boldsymbol{\delta F} = \left\langle \boldsymbol{\nabla}_{\boldsymbol{F}} \lambda, \boldsymbol{\delta F} \right\rangle, \qquad \frac{\partial \mathscr{L}}{\partial H}\delta H = \left\langle \boldsymbol{\nabla}_H \lambda, \delta H \right\rangle, \tag{A13}
$$

and

$$
\frac{\partial \mathscr{L}}{\partial \boldsymbol{U}_w}\boldsymbol{\delta U}_w = \left\langle\!\left\langle \boldsymbol{\nabla}_{\boldsymbol{U}_w} \lambda, \boldsymbol{\delta U}_w \right\rangle\!\right\rangle, \qquad \frac{\partial \mathscr{L}}{\partial T_w}\delta T_w = \left\langle\!\left\langle \boldsymbol{\nabla}_{T_w} \lambda, \delta T_w \right\rangle\!\right\rangle . \tag{A14}
$$

We consider first the case of forcing in the bulk only, for which $\boldsymbol{\delta U}_w = \boldsymbol{0}$ and $\delta T_w = 0$. The gradient with respect to $\boldsymbol{Q}$ reads

$$
\frac{\partial \mathscr{L}}{\partial \boldsymbol{Q}}\boldsymbol{\delta Q} = -\left\langle \hat{\boldsymbol{q}}^\dagger, \frac{\partial}{\partial \boldsymbol{Q}}\big(\lambda \mathcal{B}(\boldsymbol{Q})\hat{\boldsymbol{q}} + \mathcal{A}_m(\boldsymbol{Q})\hat{\boldsymbol{q}}\big)\boldsymbol{\delta Q} \right\rangle - \left\langle \boldsymbol{Q}^\dagger, \mathcal{A}_0(\boldsymbol{Q})\boldsymbol{\delta Q} \right\rangle
$$
$$
= -\left\langle \left\{ \frac{\partial}{\partial \boldsymbol{Q}}\big(\lambda \mathcal{B}(\boldsymbol{Q})\hat{\boldsymbol{q}} + \mathcal{A}_m(\boldsymbol{Q})\hat{\boldsymbol{q}}\big) \right\}^\dagger \hat{\boldsymbol{q}}^\dagger, \boldsymbol{\delta Q} \right\rangle - \left\langle \mathcal{A}_0^\dagger(\boldsymbol{Q})\boldsymbol{Q}^\dagger, \boldsymbol{\delta Q} \right\rangle . \tag{A15}
$$

Cancelling this gradient, we obtain that the adjoint base flow $\boldsymbol{Q}^\dagger$ is solution of the non-degenerate, linear, non-homogeneous problem reading

$$
\mathcal{A}_0^\dagger(\boldsymbol{Q})\boldsymbol{Q}^\dagger = -\left\{ \frac{\partial}{\partial \boldsymbol{Q}}\big(\lambda \mathcal{B}(\boldsymbol{Q})\hat{\boldsymbol{q}} + \mathcal{A}_m(\boldsymbol{Q})\hat{\boldsymbol{q}}\big) \right\}^\dagger \hat{\boldsymbol{q}}^\dagger = \boldsymbol{\nabla}_{\boldsymbol{Q}} \lambda , \tag{A16}
$$

with $\mathcal{A}_0^\dagger$ the adjoint operator for the axisymmetric linearized operator $\mathcal{A}_0$. One recognizes in the right-hand side the sensitivity to base flow modifications which turns out to be a prerequisite for the present analysis. The boundary conditions to be fulfilled by the adjoint base flow are such that all boundary terms arising during the integration are zero. Admissible variations are such that $\boldsymbol{\delta U} = \boldsymbol{0}$ and $\delta T = 0$ on Γ_c. In the unforced case solved in the present study, the condition on the control surface Γ_c therefore reads $\boldsymbol{U}^\dagger = \boldsymbol{0}$, $T^\dagger = 0$. Since the gradients with respect to the control variables J, $\boldsymbol{F}$ and H are simply given by

$$
\frac{\partial \mathscr{L}}{\partial J}\delta J = \left\langle \rho^\dagger, \delta J \right\rangle, \qquad \frac{\partial \mathscr{L}}{\partial \boldsymbol{F}}\boldsymbol{\delta F} = \left\langle \boldsymbol{U}^\dagger, \boldsymbol{\delta F} \right\rangle, \qquad \frac{\partial \mathscr{L}}{\partial H}\delta H = \left\langle T^\dagger, \delta H \right\rangle, \tag{A17}
$$

it can be deduced from $(A13)$ that $\boldsymbol{\nabla}_J \lambda = \rho^\dagger$, $\boldsymbol{\nabla}_{\boldsymbol{F}} \lambda = \boldsymbol{U}^\dagger$ and $\boldsymbol{\nabla}_H \lambda = T^\dagger$.

We add now the forcing at the wall. The gradient with respect to $\boldsymbol{Q}$ now reads

$$
\begin{aligned}
\frac{\partial \mathscr{L}}{\partial \boldsymbol{Q}} \delta \boldsymbol{Q} &= -\left\langle \hat{\boldsymbol{q}}^\dagger,\, \frac{\partial}{\partial \boldsymbol{Q}}\big(\lambda \mathcal{B}(\boldsymbol{Q})\hat{\boldsymbol{q}} + \mathcal{A}_m(\boldsymbol{Q})\hat{\boldsymbol{q}}\big)\delta \boldsymbol{Q} \right\rangle - \left\langle \boldsymbol{Q}^\dagger,\, \mathcal{A}_0(\boldsymbol{Q})\delta\boldsymbol{Q} \right\rangle \\
&\quad -\left\langle\!\!\left\langle \boldsymbol{U}_w^\dagger,\, \boldsymbol{\delta U} \right\rangle\!\!\right\rangle - \left\langle\!\!\left\langle T_w^\dagger,\, \delta T \right\rangle\!\!\right\rangle \tag{A18a}
\end{aligned}
$$

$$
\begin{aligned}
&= \underbrace{-\left\langle \left\{\frac{\partial}{\partial \boldsymbol{Q}}\big(\lambda \mathcal{B}(\boldsymbol{Q})\hat{\boldsymbol{q}} + \mathcal{A}_m(\boldsymbol{Q})\hat{\boldsymbol{q}}\big)\right\}^\dagger \hat{\boldsymbol{q}}^\dagger,\, \delta\boldsymbol{Q} \right\rangle - \left\langle \mathcal{A}_0^\dagger(\boldsymbol{Q})\boldsymbol{Q}^\dagger,\, \delta\boldsymbol{Q} \right\rangle}_{(i)} \\
&\quad \underbrace{-\left\langle\!\!\left\langle \boldsymbol{U}_w^\dagger,\, \boldsymbol{\delta U} \right\rangle\!\!\right\rangle - \left\langle\!\!\left\langle T_w^\dagger,\, \delta T \right\rangle\!\!\right\rangle}_{(ii)} + \text{ BT} \tag{A18b}
\end{aligned}
$$

Since $\boldsymbol{Q}^\dagger$ is solution of $(A16)$, the term (i) in $(A18b)$ is zero. However, admissible variations on Γ_c are now such that $\boldsymbol{\delta U} = \boldsymbol{\delta U}_w$ and $\delta T = \delta T_w$, so that the boundary term BT arising during the integration is not zero anymore. Cancellation of the term (ii) in $(A18b)$ thus yields the definition of the adjoint wall quantities $\boldsymbol{U}_w^\dagger$ and $T_w^\dagger$ as

$$
\boldsymbol{U}_w^\dagger = \rho\rho^\dagger \boldsymbol{n} + \frac{1}{Re}\boldsymbol{\tau}(\boldsymbol{U}^\dagger)\cdot\boldsymbol{n}\,, \qquad T_w^\dagger = \frac{\gamma}{PrRe}\boldsymbol{\nabla}T^\dagger\cdot\boldsymbol{n}\,. \tag{A19}
$$

Since the gradients with respect to $\boldsymbol{U}_w$ and T_w are simply given by

$$
\frac{\partial \mathscr{L}}{\partial \boldsymbol{U}_w}\boldsymbol{\delta U}_w = \left\langle\!\!\left\langle \boldsymbol{U}_w^\dagger,\, \boldsymbol{\delta U}_w \right\rangle\!\!\right\rangle\,, \qquad \frac{\partial \mathscr{L}}{\partial T_w}\delta T_w = \left\langle\!\!\left\langle T_w^\dagger,\, \delta T_w \right\rangle\!\!\right\rangle\,, \tag{A20}
$$

it can be deduced from $(A14)$ that $\boldsymbol{\nabla}_{\boldsymbol{U}_w}\lambda = \boldsymbol{U}_w^\dagger$ and $\boldsymbol{\nabla}_{T_w}\lambda = T_w^\dagger$.

3. Link between both approaches

Both approaches are connected through the base flow modification $\boldsymbol{\delta Q}$ induced by the variation of the forcing terms. $\boldsymbol{\delta Q}$ is solution of the linear problem

$$
\mathcal{A}_0\boldsymbol{\delta Q} = (\delta J, \boldsymbol{\delta F}, \delta H, 0)^T\,, \tag{A21}
$$

along with the boundary conditions $\boldsymbol{\delta U} = \boldsymbol{\delta U}_w$ and $\delta T = \delta T_w$ on Γ_c. The eigenvalue modification $\delta\lambda$ can be expressed in the framework of the sensitivity to base flow modifications as

$$
\delta\lambda = \left\langle \boldsymbol{\nabla}_{\boldsymbol{Q}}\lambda,\, \boldsymbol{\delta Q} \right\rangle\,. \tag{A22}
$$

Using $(A16) - (A18)$ and $(A21)$, this relation turns into

$$
\delta\lambda = \left\langle \mathcal{A}_0^\dagger\boldsymbol{Q}^\dagger,\, \boldsymbol{\delta Q} \right\rangle = \left\langle \boldsymbol{Q}^\dagger,\, \mathcal{A}_0\boldsymbol{\delta Q} \right\rangle + \text{BT} = \left\langle \boldsymbol{Q}^\dagger,\, (\delta J, \boldsymbol{\delta F}, \delta H, 0)^T \right\rangle + \text{BT}\,. \tag{A23}
$$

Since the term (ii) in A18(b) is zero, and using the expressions of the sensitivity functions to a bulk forcing derived in Sec. A 2, we obtain finally

$$
\delta\lambda = \left\langle \boldsymbol{\nabla}_J\lambda, \delta J \right\rangle + \left\langle \boldsymbol{\nabla}_{\boldsymbol{F}}\lambda, \boldsymbol{\delta F} \right\rangle + \left\langle \boldsymbol{\nabla}_H\lambda, \delta H \right\rangle + \left\langle\!\!\left\langle \boldsymbol{\nabla}_{\boldsymbol{U}_w}\lambda, \boldsymbol{\delta U}_w \right\rangle\!\!\right\rangle + \left\langle\!\!\left\langle \boldsymbol{\nabla}_{T_w}\lambda, \delta T_w \right\rangle\!\!\right\rangle\,, \tag{A24}
$$

and retrieve the variation (16) defined formally in the framework of the sensitivity to steady forcing.

Appendix B: DETAILED EXPRESSION OF THE DIFFERENTIAL OPERATORS

All operators pertain here to the state vector $\boldsymbol{q} = (\rho, \boldsymbol{u}, T, p)^T$. The reduced form used in the numerics, pertaining to the state vector $\boldsymbol{q} = (\rho, \boldsymbol{u}, T)^T$, can be straightforwardly deduced by replacing

the pressure terms by their expression issuing from the perfect gas state equation. $\mathcal{I}$ being the identity operator, the non-zero components of operators $\mathcal{B}$, $\mathcal{A}_m$ and $\mathcal{C}_m$ governing the dynamics of the direct modes read

$$\mathcal{B}_{11} \quad = 1 \, ,$$
$$\mathcal{B}_{22} \quad = \rho \mathcal{I} \, ,$$
$$\mathcal{B}_{33} \quad = \rho \, ,$$

$$\mathcal{A}_{m\,11} = \boldsymbol{U} \cdot \boldsymbol{\nabla} + \boldsymbol{\nabla} \cdot \boldsymbol{U} \, ,$$
$$\mathcal{A}_{m\,12} = \boldsymbol{\nabla}\rho \cdot + \rho \boldsymbol{\nabla} \cdot \, ,$$
$$\mathcal{A}_{m\,21} = \boldsymbol{\nabla U} \cdot \boldsymbol{U} \, ,$$
$$\mathcal{A}_{m\,22} = \rho \boldsymbol{\nabla}[\bullet] \cdot \boldsymbol{U} + \rho \boldsymbol{\nabla U} \cdot [\bullet] - \frac{1}{Re} \boldsymbol{\nabla} \cdot \boldsymbol{\tau}[\bullet] \, ,$$
$$\mathcal{A}_{m\,24} = \frac{1}{\gamma M^2} \boldsymbol{\nabla} \, ,$$
$$\mathcal{A}_{m\,31} = \boldsymbol{U} \cdot \boldsymbol{\nabla} T \, ,$$
$$\mathcal{A}_{m\,32} = \rho \boldsymbol{\nabla} T \cdot + (\gamma - 1)P\boldsymbol{\nabla} \cdot - \gamma(\gamma - 1)\frac{M^2}{Re} \left(\boldsymbol{\tau}(\boldsymbol{U}) : \boldsymbol{d}[\bullet] + \boldsymbol{\tau}[\bullet] : \boldsymbol{d}(\boldsymbol{U}) \right) \, ,$$
$$\mathcal{A}_{m\,33} = \rho \boldsymbol{U} \cdot \boldsymbol{\nabla} - \frac{\gamma}{PrRe} \boldsymbol{\nabla}^2 \, ,$$
$$\mathcal{A}_{m\,34} = (\gamma - 1)\boldsymbol{\nabla} \cdot \boldsymbol{U} \, ,$$
$$\mathcal{A}_{m\,41} = -T \, ,$$
$$\mathcal{A}_{m\,43} = -\rho \, ,$$
$$\mathcal{A}_{m\,44} = 1, \, .$$

$$\mathcal{C}_{m\,11} = \boldsymbol{U} \cdot \boldsymbol{\nabla} + \boldsymbol{\nabla} \cdot \boldsymbol{U} \, ,$$
$$\mathcal{C}_{m\,21} = \boldsymbol{\nabla U} \cdot \boldsymbol{U} \, ,$$
$$\mathcal{C}_{m\,22} = \rho \boldsymbol{\nabla}[\bullet] \cdot \boldsymbol{U} \, ,$$
$$\mathcal{C}_{m\,31} = \boldsymbol{U} \cdot \boldsymbol{\nabla} T \, ,$$
$$\mathcal{C}_{m\,33} = \rho \boldsymbol{U} \cdot \boldsymbol{\nabla} \, .$$

Similarly, the non-zero terms of the adjoint operators $\mathcal{A}_m^\dagger$ and $\mathcal{C}_m^\dagger$ governing the dynamics of the adjoint modes read

$$\mathcal{A}^\dagger_{m\,11} = -\boldsymbol{U} \cdot \boldsymbol{\nabla} \,,$$

$$\mathcal{A}^\dagger_{m\,12} = (\boldsymbol{\nabla U} \cdot \boldsymbol{U}) \cdot \,,$$

$$\mathcal{A}^\dagger_{m\,13} = \boldsymbol{U} \cdot \boldsymbol{\nabla} T \,,$$

$$\mathcal{A}^\dagger_{m\,14} = -T \,,$$

$$\mathcal{A}^\dagger_{m\,21} = -\rho \boldsymbol{\nabla} \,,$$

$$\mathcal{A}^\dagger_{m\,22} = -\rho \boldsymbol{\nabla}[\bullet] \cdot \boldsymbol{U} + \rho \boldsymbol{\nabla U}^T \cdot - \frac{1}{Re} \boldsymbol{\nabla} \cdot \boldsymbol{\tau}[\bullet] \,,$$

$$\mathcal{A}^\dagger_{m\,23} = \rho \boldsymbol{\nabla} T - (\gamma - 1) \boldsymbol{\nabla}(P[\bullet]) + 2\gamma(\gamma-1)\frac{M^2}{Re}\boldsymbol{\nabla} \cdot ([\bullet]\boldsymbol{\tau}(\boldsymbol{U})) \,,$$

$$\mathcal{A}^\dagger_{m\,33} = -\rho \boldsymbol{U} \cdot \boldsymbol{\nabla} - \frac{\gamma}{PrRe}\boldsymbol{\nabla}^2 \,,$$

$$\mathcal{A}^\dagger_{m\,34} = -\rho \,,$$

$$\mathcal{A}^\dagger_{m\,42} = -\frac{1}{\gamma M^2}\boldsymbol{\nabla} \cdot \,,$$

$$\mathcal{A}^\dagger_{m\,43} = (\gamma - 1)\boldsymbol{\nabla} \cdot \boldsymbol{U} \,,$$

$$\mathcal{A}^\dagger_{m\,44} = 1 \,,$$

$$\mathcal{C}^\dagger_{m\,11} = -\boldsymbol{U} \cdot \boldsymbol{\nabla} \,,$$

$$\mathcal{C}^\dagger_{m\,12} = (\boldsymbol{\nabla U} \cdot \boldsymbol{U}) \cdot \,,$$

$$\mathcal{C}^\dagger_{m\,13} = \boldsymbol{U} \cdot \boldsymbol{\nabla} T \,,$$

$$\mathcal{C}^\dagger_{m\,22} = -\rho \boldsymbol{\nabla}[\bullet] \cdot \boldsymbol{U} \,,$$

$$\mathcal{C}^\dagger_{m\,33} = -\rho \boldsymbol{U} \cdot \boldsymbol{\nabla}$$

Finally, operator $\mathcal{A}^\dagger_0$ is obtained simply by taking the axisymmetric form of operator $\mathcal{A}^\dagger_m$.

---

[1] S.G. Siegel and H.F. Fasel, "Effect of forcing on the wake drag of an axisymmetric bluff body", AIAA Paper 2001-0736 (2001).

[2] Seidel, J. and Siegel, S. and Jeans T. and Aradag, S. and Cohen, K. and McLaughlin, T., "Analysis of an axisymmetric bluff body wake using Fourier transform and POD", AIAA Paper 2008-552 (2008).

[3] Siegel, S. and Seidel, J. and Cohen, K. and Aradag, S. and McLaughlin, T., "Open loop transient forcing of an axisymmetric bluff body wake", AIAA Paper 2008-595 (2008).

[4] E. Achenbach, "Experiments on the flow past spheres at very high Reynolds numbers", J. Fluid Mech. **54** 565 (1972).

[5] S. Taneda, "Visual observations of the flow past a sphere at Reynolds numbers between 10^4 and 10^6", J. Fluid Mech. **85** 187 (1978).

[6] D. Deprés, P. Reijasse and J.-P. Dussauge, "Analysis of unsteadiness in afterbody transonic flows", AIAA Journal **42** 2541 (2004).

[7] H. Choi, W.-P. Jeon and J. Kim, "Control of flow over a bluff body", Annu. Rev. Fluid Mech. **40** 113 (2008).

[8] P.J. Strykowski and K.R. Sreenivasan, "On the formation and suppression of vortex shedding at 'low' Reynolds numbers", Annu. Rev. Fluid Mech. **218** 71 (1990).

[9] H. Illy, P. Geffroy and L. Jacquin, "Control of cavity flow by means of a spanwise cylinder", Proc. 21st International Congress on Theoretical and Applied Mechanics, Warsaw (2004).

[10] W.A. Mair, "The effect of a rear-mounted disc on the drag of a blunt-based body of revolution", Aeronaut. Q. **16** 350 (1965).

[11] A. Weickgenannt and P.A. Monkewitz, "Control of vortex shedding in an axisymmetric bluff body wake", Eur. J. Mech. B/Fluids **19** 789 (2000).

[12] P.-Q. Elias, B. Chanetz, S. Larigaldie, D. Packan and C.O. Laux, "Mach 3 shock wave unsteadiness alleviation using a negative corona discharge", AIAA Journal **46** 2042 (2008).

[13] W. Bearman, "The effect of base bleed on the flow behind a twodimensional model with a blunt trailing edge", Aeronaut. Q. **18** 207 (1967).

[14] G. Leal and A. Acrivos, "The effect of base bleed on the steady separated flow past bluff objects", J. Fluid Mech. **39** 735 (1969).

[15] N.S. Diaconis, J.R. Jack and R.J. Wisniewski, "Boundary-layer transition at Mach 3.12 as affected by cooling and nose blunting", NASA Tech. Rep. **3928** (1957).

[16] J.R. Jack, R.J. Wisniewski and N.S. Diaconis, "Effects of extreme surface cooling on boundary-layer transition", NASA Tech. Rep. **4094** (1957).

[17] P. Klebanoff, G. Schubauer and K. Tidstrom, "Measurements of the effect of two-dimensional and three-dimensional roughness elements on boundary-layer transition", J. Aero. Sci. **22** 803 (1955).

[18] E. Moreau, "Airflow control by non-thermal plasma actuators", Jour. Phys. D **40** 605 (2007).

[19] C.P. Jackson, "A finite-element study of the onset of vortex shedding in flow past variously shaped bodies", J. Fluid Mech. **182** 23 (1987).

[20] A. Zebib, "Stability of a viscous flow past a circular cylindar", J. Engng Math. **21** 155 (1987).

[21] V. Theofilis, "Advances in global linear instability analysis of nonparallel and three-dimensional flows", Prog. Aerospace Sci. **39** 249 (2003).

[22] S. S. Collis, R.D. Joslin, A. Seifert and V. Theofilis, "Issues in active flow control: theory, control, simulation, and experiment", Prog. Aerospace Sci. **40** 237 (2004).

[23] D.C. Hill, "A theoretical approach for analyzing the restabilization of Wakes", NASA Tech. Rep. **103858** (1992).

[24] O. Marquet, D. Sipp and L. Jacquin, "Sensitivity analysis and passive control of the cylinder flow", J. Fluid Mech. **615** 221 (2008).

[25] F. Giannetti and P. Luchini, "Structural sensitivity of the first instability of the cylinder wake", J. Fluid Mech. **581** 167 (2007).

[26] J.O. Pralits, C. Airiau, A. Hanifi and D.S. Henningson, "Sensitivity analysis using adjoint parabolized stability equations for compressible flows", Flow, Turb. Comb. **65** 321 (2000).

[27] P. Meliga, "A theoretical approach for the onset and control of unsteadiness in compressible afterbody flows", PhD thesis, École Polytechnique (2008).

[28] T.R. Bewley, R. Temam and M. Ziane, "A general framework for robust control in fluid mechanics", Physica D **138** 363 (2000).

[29] A. Sevilla and C. Martínez-Bazàn, "Vortex shedding in high Reynolds number axisymmetric bluff-body wakes: Local linear instability and global bleed control", Phys. Fluids **16** 3460 (2004).

[30] J.D. Crouch, A. Garbaruk, D. Magidov and A. Travin, "Origin of transonic buffet on aerofoils", J. Fluid Mech. **628** 357 (2009).

[31] T. Colonius, "Modeling artificial boundary conditions for compressible flow", Annu. Rev. Fluid Mech. **36** 315 (2004).

[32] J. Matsumoto and M. Kawahara, "Stable shape identification for fluid-structure interaction problem using MINI element", J. Appl. Mech. **3** 263 (2000).

[33] D. Barkley, M.G.M. Gomes and R.D. Henderson, "Three-dimensional instability in flow over a backward-facing step", J. Fluid Mech. **473** 167 (2002).

[34] T.A. Davis and I.S. Duff, "An unsymmetric-pattern multifrontal method for sparse lu factorization", SIAM Journal on Matrix Analysis and Applications **18** 140 (1997).

[35] T.A. Davis, "A column pre-ordering strategy for the unsymmetric-pattern multifrontal method", ACM Transactions on Mathematical Software **30** 165 (2004).

[36] J.W. Nichols, P.J. Schmid and J.J. Riley, "Self-sustained oscillations in variable-density round jets", J. Fluid Mech. **582** 341 (2007).

[37] P. Meliga, J.-M. Chomaz and D. Sipp, "Global mode interaction and pattern selection in the wake of a disk: a weakly nonlinear expansion", J. Fluid Mech. **633** 159 (2009).

[38] S. Lee, S.K. Lele and P. Moin, "Direct numerical simulation of isotropic turbulence interacting with a weak shock wave", J. Fluid Mech. **251** 533 (1993).

[39] B. Fornberg, "Steady viscous flow past a sphere at high Reynolds number", J. Fluid Mech. **190** 471 (1988).

[40] R. Natarajan and A. Acrivos, "The instability of the steady flow past spheres and disks", J. Fluid Mech. **254** 323 (1993).

[41] U. Ehrenstein and F. Gallaire, "On two-dimensional temporal modes in spatially evolving open flows: the flat-plate boundary layer", J. Fluid Mech. **536** 209 (2005).

[42] C.W. Rowley, T. Colonius and R.M. Murray, "Model Reduction for Compressible Flows using POD and Galerkin Projection", Physica D **189** 115 (2004).

[43] T.A. Johnson and V.C. Patel, "Flow past a sphere up to a Reynolds number of 300", J. Fluid Mech. **378** 19 (1999).

[44] D. Fabre, F. Auguste and J. Magnaudet, "Bifurcations and symmetry breaking in the wake of axisymmetric bodies", Phys. Fluids **20** 051702 (2008).

[45] F. Giannetti and P. Luchini, "Receptivity of the circular cylinders first instability", Proc. 5th European

Fluid Mechanics Conference, Toulouse (2003).

[46] J.-M. Chomaz, "Global instabilities in spatially developing flows: Non-normality and nonlinearity", Annu. Rev. Fluid. Mech. **37** 357 (2005).

[47] M.D. Gunzburger, "Sensitivities, adjoints and flow optimization", Int. J. Numer. Meth. Fluids **31** 53 (1999).

[48] C. Airiau, A. Bottaro, S. Walther and D. Legendre, "A methodology for optimal laminar flow control: Application to the damping of Tollmien-Schlichting waves in a boundary layer", Phys. Fluids **15** 1131 (2003).

[49] O. Marquet, D. Sipp, L. Jacquin and J.-M. Chomaz, "Multiple timescale and sensitivity analysis for the passive control of the cylinder flow", AIAA Paper 2008-4228 (2008).

[50] A. Bottaro, P. Corbett and P. Luchini, "The effect of base flow variation on flow stability", J. Fluid Mech. **476** 293 (2003).

[51] Y. Hwang and H. Choi, "Control of absolute instability by basic-flow modification in parallel wake at low Reynolds number", J. Fluid Mech. **560** 465 (2006).

[52] P.J. Schmid and D.S. Henningson, "Stability and transition in shear flows", Springer-Verlag, New York (2001).

http://www.freefem.org

http://www.cise.ufl.edu/research/sparse/UMFPACK

http://www.caam.rice.edu/software/ARPACK